

1 Higgs boson mass and model-independent ZH
2 cross-section at FCC-ee in the di-electron and
3 di-muon final states

4 Ang Li^{1*}, Jan Eysermans² and Gregorio Bernardi¹

5 ^{1*} Laboratoire AstroParticule et Cosmologie, CNRS/IN2P3, 10, Rue
6 Alice Domon et Léonie Duquet, Paris, 75013, France .

7 ² Particle Physics Collaboration, Massachusetts Institute of Technology,
8 77 Massachusetts Ave, Boston, Cambridge, 02139, MA, USA .

9 *Corresponding author(s). E-mail(s): ang.l@cern.ch;

10 Contributing authors: jan.eysermans@cern.ch;
11 gregorio.bernardi@cern.ch;

12 This note outlines the prospects of Higgs boson mass and model-independent ZH
13 cross-section measurements at the FCC-ee, using the recoil mass method, at $\sqrt{s} = 240$
14 GeV. The two analyses, which use selections based on kinematic requirements and
15 advanced techniques are described. The statistical interpretation of the di-muon and
16 di-electron channels are presented separately and then combined. The results are then
17 discussed within the targeted experimental conditions such as detector configurations
18 and machine parameters.

19	Contents	
20	1 Introduction	4
21	1.1 Motivation	4
22	1.2 "Recoil mass" method	6
23	2 Monte Carlo samples	9
24	2.1 Event generators	9
25	2.2 Muon and electron performance	14
26	3 Event selection	15
27	3.1 Preselection cuts	15
28	3.2 Kinematic cuts	16
29	3.3 Basic and Baseline selections	16
30	3.4 Event yields and cut flow	16
31	4 Higgs mass measurement	19
32	4.1 Event categorization	19
33	4.2 Signal modeling	20
34	4.3 Background modeling	22
35	4.4 Results	23
36	4.5 Auxiliary fits	25
37	5 ZH cross-section measurement	27
38	5.1 Boosted Decision Tree	28
39	5.1.1 Training samples	28
40	5.1.2 Input variables	29
41	5.1.3 Hyper-parameters	30
42	5.1.4 BDT Performance	30
43	5.2 Fitting strategy	35
44	5.2.1 Fit on recoil mass distribution	35
45	5.2.2 Fit on BDT score distribution	37
46	5.3 Conclusion	39
47	6 Sources of systematic uncertainties	40
48	6.1 Beam Energy Spread (BES)	40
49	6.2 Initial State Radiation (ISR)	42
50	6.2.1 ISR treatment in WHIZARD	42
51	6.2.2 Comparison with KKMC	43
52	6.3 Center-of-mass (COM)	44
53	6.4 Lepton momentum scale (LEPSCALE)	44
54	6.5 Lepton momentum resolution (LEPRES)	46
55	6.6 Final State Radiation (FSR)	46
56	6.7 Signal modeling (SIGM)	46
57	6.8 Background modeling (BKGM)	46
58	7 Experimental requirements	47

59	8 Conclusion	48
60	A Event selection plots	49
61	B Recoil mass fits	51
62	C BDT input variables	53
63	D BDT hyper-parameters	55

1 Introduction

1.1 Motivation

The FCCee (Future Circular Collider in the Electron-Positron collision mode) is designed to operate at several center-of-mass energies, denoted as \sqrt{s} , to develop a rich physics programme [1]. In particular, it will run at $\sqrt{s} = 240$ GeV, where it is expected to generate approximately 10^6 $e^+ + e^- \rightarrow ZH$ events in four years of data taking. Although VH events have been previously observed in the ATLAS detector [2] and CMS [3], the significantly larger number of ZH events produced by the FCCee, and the much smaller background will enable unprecedented precision in the measurement of Higgs boson properties.

At $\sqrt{s} = 240$ GeV, the main Higgs production modes are the "Higgsstrahlung" process, $e^+ + e^- \rightarrow ZH$, and to a lesser extent, the WW fusion process, $e^+ + e^- \rightarrow \nu_e \bar{\nu}_e H$, as shown in Figure 1.

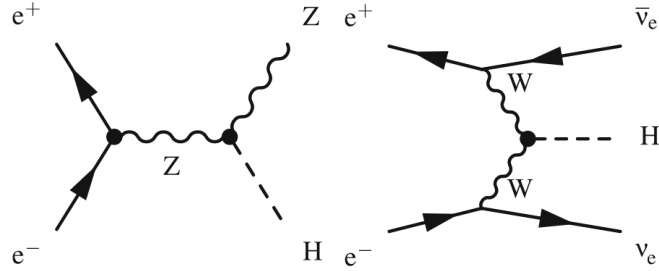


Fig. 1 Main diagrams of the Higgs production modes at $\sqrt{s} = 240$ GeV: the Higgsstrahlung process (left) and the WW fusion process (right). Adapted from Ref. [4].

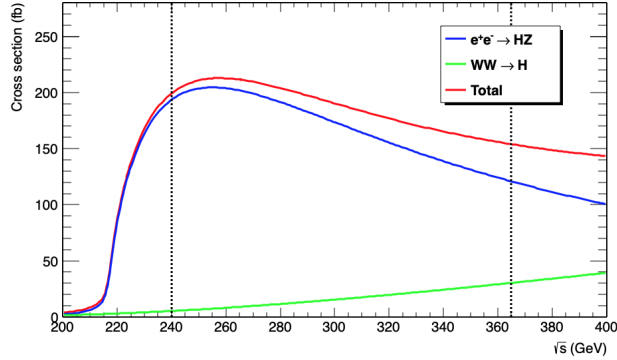


Fig. 2 Improved-Born Higgs production cross sections for the Higgsstrahlung process and the WW fusion process (see Figure 1), incorporating initial state radiation [5], are predicted by HZHA [6] as a function of center-of-mass energy with a Higgs boson mass m_h of 125 GeV. The minor interference term between the two diagrams in the final state is integrated into the WW fusion cross-section. Vertical dashed lines represent the anticipated \sqrt{s} values at the FCC-ee. Adapted from Ref. [4].

In comparison to hadron collisions, electron-positron collisions offer the unique advantage of knowing the precise center-of-mass energy for each event. In hadron colliders, the initial momentum of the interacting gluons or quarks remains unknown, necessitating the use of parton distribution functions. Conversely, electron-positron colliders involve collisions between elementary particles—electrons and positrons—thereby eliminating the need for parton distribution functions and enabling a more accurate understanding of the initial conditions of the binary system. Consequently, electron-positron machines serve as ideal candidates for conducting precise measurements in the realm of particle physics.

In Higgsstrahlung events, since the center-of-mass energy of the collision is known, we can acquire information on the recoiling Higgs boson, just by studying the associated Z boson, as detailed in Section 1.2. This boson comprises a pair of leptons ($\ell^+\ell^-$) or quarks ($q\bar{q}$) and does not require prior knowledge of the Higgs information. Consequently, we can carry out a Higgs model-independent study.

By quantifying the number of events related to Higgsstrahlung and WW fusion processes, we can ascertain their respective inclusive cross-sections. Examining the distribution of the recoil mass (m_{rec}) allows us to extract the Higgs mass with uncertainty at the MeV level.

We can analyze various Higgs decay modes ($H \rightarrow X\bar{X}$). The cross-section times the branching ratio is proportional to the square of the respective coupling strengths. This relationship can be expressed as follows:

$$\sigma_{\text{ZH}} \times Br(H \rightarrow X\bar{X}) \propto \frac{g_{HZZ}^2 \times g_{HXX}^2}{\Gamma_H}, \quad (1)$$

$$\sigma_{H\nu_e\bar{\nu}_e} \times Br(H \rightarrow X\bar{X}) \propto \frac{g_{HWW}^2 \times g_{HXX}^2}{\Gamma_H}. \quad (2)$$

Here, σ_{ZH} and $\sigma_{H\nu_e\bar{\nu}_e}$ represent the inclusive cross-sections of the Higgsstrahlung and WW fusion processes, respectively. $Br(H \rightarrow X\bar{X})$ denotes the branching ratio of Higgs decays into an $X\bar{X}$ particle pair, which can be any known or unknown particle. g_{HXX} is the Higgs coupling constant, and Γ_H is the Higgs width. Equation 1 demonstrates the proportionality for the ZH production process, while Equation 2 illustrates the proportionality for the $\nu_e\bar{\nu}_e H$ production process.

By analyzing the Higgs boson decay to a pair of Z boson, $H \rightarrow ZZ$, we can extract the Higgs coupling to two Z bosons, denoted as g_{HZZ} . This coupling can be determined from Equation 1 $\sigma_{\text{ZH}} \times Br(H \rightarrow ZZ) \propto \frac{g_{HZZ}^4}{\Gamma_H}$. Once obtained, g_{HZZ} serves as a "standard candle" to facilitate the study of other Higgs decay channels. This approach allows us to determine all the Higgs couplings, g_{HXX} , thereby providing a comprehensive understanding of the Higgs boson's properties and its interactions with other particles.

111 The Higgs mass is a fundamental parameter of the Standard Model (SM) and will
 112 be measured by the HL-LHC up to a precision of 20 MeV [7]. Although radiative
 113 corrections to all other SM only depends logarithmically on m_h , to fully exploit the
 114 FCC-ee potential in measuring the cross-sections and branching fractions, the Higgs
 115 mass has to be known up to a 10 MeV level. Furthermore, a potential run at the Higgs
 116 resonance of $\sqrt{s} = 125$ GeV can probe the electron-Yukawa coupling via s-channel
 117 Higgs production and requires precision of the Higgs mass equal or better to its width,
 118 i.e. around 4 MeV [8].

119 Both the cross-section and mass measurements are challenging and put stringent
 120 requirements on the detector and machine parameters, which is the scope of this note.
 121 It extends the initial studies as described in Ref. [4], to a more complete analysis with
 122 a robust evaluation of the uncertainties.

123 1.2 "Recoil mass" method

124 In this section, we remind the technical aspects of the recoil technique, for the final
 125 state that study: we focus on the leptonic decays of the Z boson ($Z \rightarrow \ell^+ \ell^-$, where $\ell = e$
 126 or μ) for mass and cross-section measurements. This choice offers greater precision
 127 and enables inclusive and efficient selection of ZH events, regardless of the Higgs
 128 boson decay mode. As a result, this method effectively facilitates an almost entirely
 129 model-independent determination of the HZZ coupling (g_{HZZ}). However, the small Z
 130 di-electron and di-muon branching ratios, Table 1, reduce the statistical accuracy but
 131 allow for better resolution.

Table 1 Z Decay Modes Branching Ratios, adapted from [9].

Decay Mode	Branching Ratio
$Z \rightarrow e^+ e^-$	$3.3632 \pm 0.0042\%$
$Z \rightarrow \mu^+ \mu^-$	$3.3662 \pm 0.0066\%$
$Z \rightarrow \tau^+ \tau^-$	$3.3696 \pm 0.0083\%$
$Z \rightarrow \text{invisible}$	$20.000 \pm 0.055\%$
$Z \rightarrow \text{hadrons}$	$69.911 \pm 0.056\%$
$Z \rightarrow c\bar{c}$	$12.03 \pm 0.21\%$
$Z \rightarrow b\bar{b}$	$15.12 \pm 0.05\%$

132 The mass m_{rec} recoiling against the lepton pair is calculated using total energy-
 133 momentum conservation, as represented in Equation 3 and illustrated in Figure 3 by
 134 computing the difference between the four-vector of center-of-mass energy and lepton
 135 pair system:

$$m_{\text{rec}}^2 = (\sqrt{s} - E_{\ell^+ \ell^-})^2 - p_{\ell^+ \ell^-}^2 = s - 2E_{\ell^+ \ell^-} \sqrt{s} + m_{\ell^+ \ell^-}^2. \quad (3)$$

136 Here, \sqrt{s} represents the center-of-mass energy, $E_{\ell^+ \ell^-}$ denotes the energy of the di-
 137 lepton pair, and $m_{\ell^+ \ell^-}$ refers to the invariant mass of the di-lepton pair.

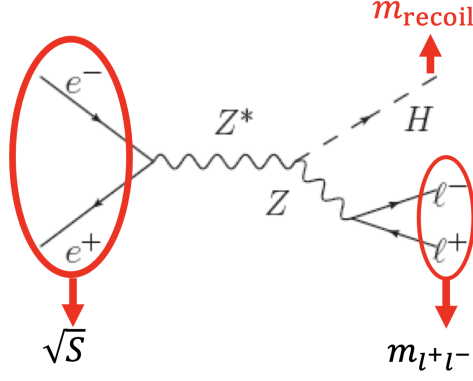


Fig. 3 Feynman diagram illustrating the Higgs-strahlung process and the recoil mass (m_{rec}) calculation. Adapted from [10].

Figure 3 provides a visual representation of the calculation using the leading order Feynman diagram of the ZH production process. Since it uses the center-of-mass energy, the recoil mass is sensitive to its precise knowledge, which can be affected by the Beam Energy Spread (BES) and Initial State Radiation (ISR) of the incoming leptons.

The main backgrounds come from the WW, ZZ, and Z/ γ processes as can be seen from Figure 4, which displays the m_{rec} distribution of both signal and background events after a basic selection described in Section 3, in the range 40 to 160 GeV. Two prominent peaks are visible: the largest one, around 91 GeV, is stemming from the ZZ process; the other one is around 125 GeV, and it originates from the $e^+ + e^- \rightarrow \text{ZH}$ process.

Figure 5 shows an example of a combined signal and background fit on the previous distribution, in the 120 to 140 GeV range. The signal modeling employs a Double-Sided Crystal Ball function, while the background representation utilizes a polynomial function. The Double-Sided Crystal Ball function features a Gaussian core, accompanied by two tails characterized by exponential functions. More details on the fitting functions will be discussed in Section 4.2.

Ultimately [4], the σ_{ZH} accuracy and the Higgs boson mass is expected to achieve 0.5% and MeV level respectively. After measuring the ZH cross-section, the couplings of HZZ, g_{HZZ} , and Higgs boson width (Γ_H) can be determined and are expected to achieve per-mil precision.

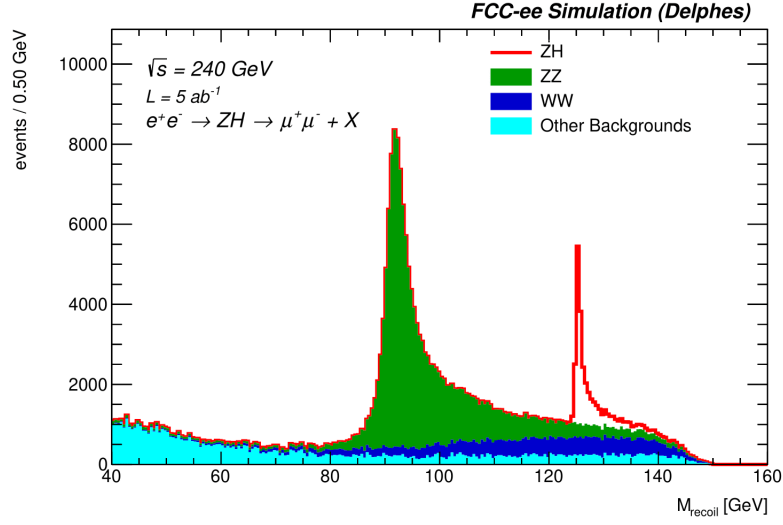


Fig. 4 Inclusive m_{rec} distribution for events where a Z boson decays into a $\mu^+\mu^-$ pair, with energies ranging from 40 to 160 GeV, after the basic selection described in Section 3. The Z and Higgs mass peaks are clearly visible in this distribution.

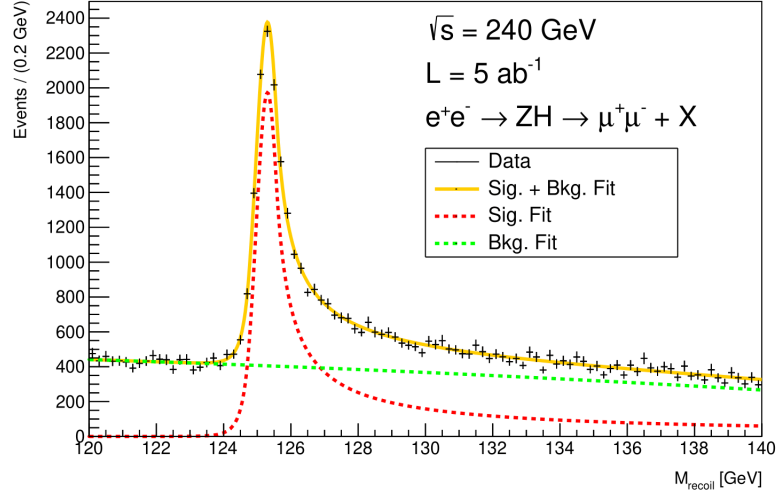


Fig. 5 Zoomed-in view of the m_{rec} distribution in the vicinity of m_h . The ZH signal is fitted using a double-sided Crystal Ball function, while the simulated background is fitted with a second-order polynomial [4].

2 Monte Carlo samples

The FCC-ee is currently in the conceptual design phase, which is conducted by feasibility studies of the physics programs using Monte Carlo (MC) simulations. These simulations enable to predict and analyze the outcomes that can be expected once the accelerator and detectors are operational.

Events for different physical processes are generated using several generators, as described in Section 2.1. The detector simulation and reconstruction are performed by the fast simulation package DELPHES [11], which smears gen-level particles with a resolution formula and efficiency to mimic a more realistic detector. The entire chain of event generation, simulation, and reconstruction is embedded within the Key4HEP software framework. The official central samples with campaign Winter2023 are used in this analysis.

For this study, the Innovative Detector for an Electron-positron Accelerator (IDEA) was selected as the default detector model for the MC simulations. Its design consists of a 5-layered silicon pixel vertex detector surrounded by a very light tracking drift chamber with up to 112 sensitive layers leading to excellent tracking performances. Both tracking devices are inside a 2 T thin solenoid. A dual-readout calorimeter is placed outside the solenoid to identify and measure both the electromagnetic and hadronic particles. Finally, the detector is enclosed by μ -RWELL muon chambers, a technology based on Resistive Plate Chambers and Gas Electron Multiplier detectors. The key feature of IDEA is to have a large tracking volume with a small yoke for optimal track resolution. In this study, a slight variant of IDEA is used, where the electromagnetic calorimeter is replaced by a crystal ECAL, improving the electron resolution significantly. An overview of the muon and electron performance is discussed in Section 2.2.

The MC samples employed in this analysis were generated at a center-of-mass energy of 240 GeV ($\sqrt{s} = 240$ GeV) using either the PYTHIA or WHIZARD generator. The luminosity in the analysis was set to 5ab^{-1} , corresponding to two interaction points. A beam energy spread of 0.185 % is applied to both incoming beams (corresponding to 222 MeV) and the vertex is smeared according to the realistic conditions, as described in the CDR [1]. The crossing angle of 30 mrad is not applied to the simulation.

2.1 Event generators

Event generation was conducted with WHIZARD [12], parton showering with PYTHIA6 [13], and both event generation and parton showering with PYTHIA8 [14]. MC samples using other generators, such as KKMC [15], were simulated to investigate systematic uncertainties. These samples are detailed in Table 2.

In this study, we consider the signal process $e^+e^- \rightarrow ZH \rightarrow \mu^+\mu^-H$ ($e^+e^- \rightarrow ZH \rightarrow e^+e^-H$) for the $\mu^+\mu^-$ (e^+e^-) final states, where the Z boson decays into a muon (electron) pair, and the Higgs boson (H) decays inclusively. The primary background sources are derived from $e^+e^- \rightarrow ZZ$, $e^+e^- \rightarrow WW$, and $e^+e^- \rightarrow \ell^+\ell^-$, with ℓ denoting either e or μ . However, Z decaying to $\tau^+\tau^-$ are always considered rare

Table 2 Monte Carlo Samples used in this analysis. They are all produced at a center-of-mass energy of 240 GeV.

Sample Name	Processes	Generator	# of events	x-section(pb)
Higgs Processes				
wzp6_ee_mumuH	$e^+e^- \rightarrow \mu^+\mu^-H$	WHIZARD + PYTHIA6	1,200,000	0.0067643
wzp6_ee_eeH	$e^+e^- \rightarrow e^+e^-H$	WHIZARD + PYTHIA6	1,200,000	0.0071611
Diboson Processes				
p8_ee_ZZ_ecm240	$e^+e^- \rightarrow ZZ$	PYTHIA8	56,162,093	1.35899
p8_ee_WW_ecm240	$e^+e^- \rightarrow WW$	PYTHIA8	373,375,386	16.4385
Dilepton Processes				
wzp6_ee_mumu	$e^+e^- \rightarrow \mu^+\mu^-$	WHIZARD + PYTHIA6	53,400,000	5.288
wzp6_ee_ee_Mee_30_150	$e^+e^- \rightarrow e^+e^-$	WHIZARD + PYTHIA6	85,400,000	8.305
wzp6_ee_tautau	$e^+e^- \rightarrow \tau^+\tau^-$	WHIZARD + PYTHIA6	52,400,000	4.668
Electron Photon Processes				
wzp6_egamma_eZ_Zmumu	$e^-\gamma \rightarrow e^-Z(\mu^+\mu^-)$	WHIZARD + PYTHIA6	6,000,000	0.10368
wzp6_gamma_eZ_Zmumu	$e^+\gamma \rightarrow e^+Z(\mu^+\mu^+)$	WHIZARD + PYTHIA6	5,600,000	0.10368
wzp6_egamma_eZ_Zee	$e^-\gamma \rightarrow e^-Z(e^+e^-)$	WHIZARD + PYTHIA6	6,000,000	0.05198
wzp6_gamma_eZ_Zee	$e^+\gamma \rightarrow e^+Z(e^+e^-)$	WHIZARD + PYTHIA6	6,000,000	0.05198
Photon Photon Processes				
wzp6_gaga_mumu_60	$\gamma\gamma \rightarrow \mu^+\mu^-$	WHIZARD + PYTHIA6	33,900,000	1.5523
wzp6_gaga_ee_60	$\gamma\gamma \rightarrow e^+e^-$	WHIZARD + PYTHIA6	22,500,000	0.873
wzp6_gaga_tautau_60	$\gamma\gamma \rightarrow \tau^+\tau^-$	WHIZARD + PYTHIA6	33,700,000	0.836
Other Processes				
wzp6_ee_nueueZ	$e^+e^- \rightarrow \nu_e\bar{\nu}_eZ$	WHIZARD + PYTHIA6	2,000,000	0.033274

backgrounds due to the low τ decay ratio to electron or muon and the presence of neutrinos in the final state which prevents the reconstructed mass to be close to the nominal Z mass.

The Feynman diagrams for all signal MC sample productions can be found in Figure 6. It illustrates the s-channel Feynman diagram of the Higgsstrahlung process, wherein the Z boson decays into various leptons (e^+e^- , $\mu^+\mu^-$, or $\tau^+\tau^-$) while the Higgs boson decays inclusively. Notably, the electron final state simulations also encompass the ZZ fusion, where Z bosons are radiated from incoming electrons or positrons, as depicted in Figure 7.

The $e^+e^- \rightarrow ZZ$ process features only t-channel Feynman diagrams, as shown in Figure 8 since the Z does not have a trilinear gauge boson vertex. The Z boson decays inclusively in this process.

In the $e^+e^- \rightarrow W^+W^-$ simulations, both s- and t-channel Feynman diagrams are included, with W decaying inclusively, as shown in Figure 9.

The $e^+e^- \rightarrow \ell^+\ell^-$ processes are represented in Figure 10 for the s-channel, with the electron final states also exhibiting a t-channel.

In a lepton collider, incoming leptons radiate photons, leading to potential interactions between the leptons and radiated photons or between the radiated photons themselves. The Feynman diagrams for electron-photon and positron-photon processes are displayed in Figure 11. These processes are characterized by $e^-(e^+)\gamma \rightarrow e^-(e^+)Z$, followed by $Z \rightarrow \ell^+\ell^-$, where ℓ can be e , μ , or τ .

Photon collisions are illustrated in the Feynman diagram in Figure 12 through the t-channel, where ℓ can be e , μ , or τ . All processes involving photon initial states are simulated using the equivalent photon/electron approximation (EPA) [16].

Figure 13 is included to comprehensively present the WW fusion processes.

In summary, this analysis focuses on the signal process $e^+e^- \rightarrow ZH \rightarrow \mu^+\mu^-H$ ($e^+e^- \rightarrow ZH \rightarrow e^+e^-H$) for the $\mu^+\mu^-$ (e^+e^-) final states, with the Z boson decaying into a muon (electron) pair and the Higgs boson decaying inclusively. The primary backgrounds considered are $e^+e^- \rightarrow ZZ$, $e^+e^- \rightarrow WW$, and $e^+e^- \rightarrow Z/\gamma$, while rare backgrounds such as $\tau^+\tau^-$ final states and the remaining backgrounds are also taken into account. Various Feynman diagrams have been generated and analyzed to understand the different processes involved and their respective contributions.

The relative size of these backgrounds after a simple requirement on the leptons can be seen in Figure 14 for both $\mu^+\mu^-$ (left) and e^+e^- channels (right).

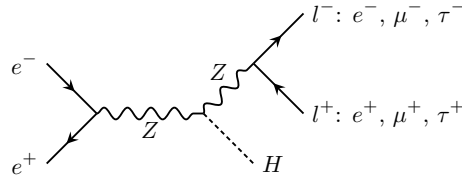


Fig. 6 Feynman diagram for the process $e^+e^- \rightarrow Z(l^+l^-)H$ where l can be e , μ or τ .

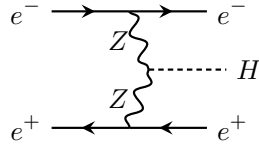


Fig. 7 Feynman diagram illustrating the $e^+e^- \rightarrow e^+e^-H$ process, where a Higgs boson is produced through the fusion of Z bosons, which are radiated from an incoming electron and positron.

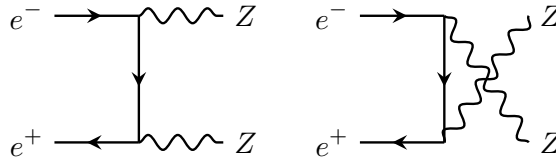


Fig. 8 Feynman diagram for the process $e^+e^- \rightarrow ZZ$, and Z decay inclusively.

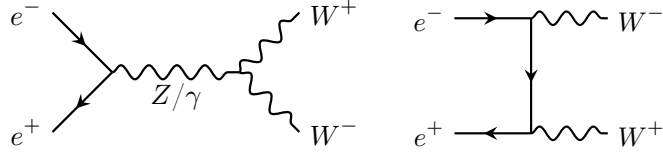


Fig. 9 Feynman diagram for the process $e^+e^- \rightarrow W^+W^-$, and W^+ and W^- decay inclusively.

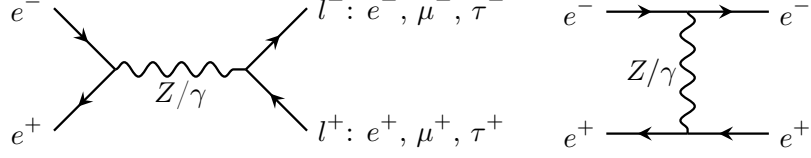


Fig. 10 Feynman diagram for the process $e^+e^- \rightarrow \ell^+\ell^-$ where ℓ can be e , μ or τ .

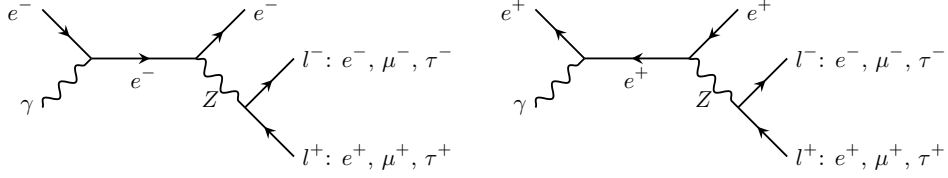


Fig. 11 Feynman diagrams for the processes $e^-\gamma \rightarrow e^-Z(\ell^+\ell^-)$ and $e^+\gamma \rightarrow e^+Z(\ell^+\ell^-)$ where ℓ can be e , μ or τ .

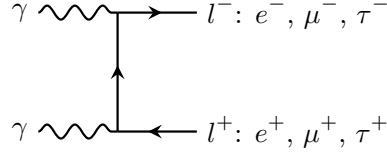


Fig. 12 Feynman diagram for the process $\gamma\gamma \rightarrow \ell^+\ell^-$ where ℓ can be e , μ or τ .

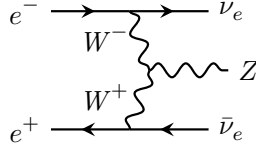


Fig. 13 Feynman diagram for the process $e^+e^- \rightarrow \nu_e\bar{\nu}_e Z$ with W exchange only to avoid double counting with ZZ inclusive process.

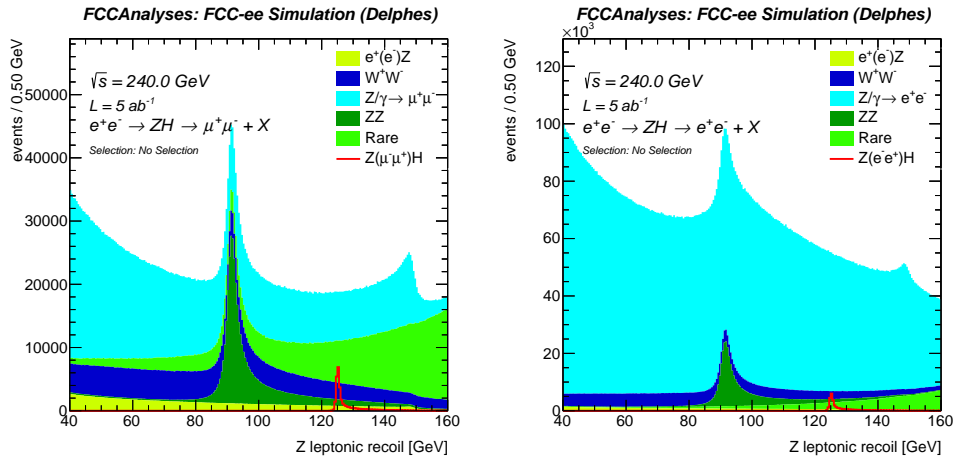


Fig. 14 m_{rec} distribution without selection for $\mu^+\mu^-$ (left) and e^+e^- (right) channels.

2.2 Muon and electron performance

The IDEA drift chamber is very light, up to 5 % X_0 in the central region and 10 % X_0 in the forward region, as can be seen from Figure 15 (left). The corresponding muon momentum resolution as a function of the momentum and azimuthal angle θ is shown on the right of Figure 15. Excellent performance is achieved with resolutions better than 0.1 %.

Electrons are subjected to Bremsstrahlung and therefore have degraded performance. However, the Bremsstrahlung photons can be detected in the ECAL and part of the energy can be recovered. Especially with the crystal ECAL, the energy recovery is maximized. Full simulation studies have shown that the equivalent degradation of electron tracks in the IDEA+crystal detector amounts to a factor of 1.25 w.r.t. the muon track resolution¹. The factor 1.25 is applied to the DELPHES simulation for electrons.

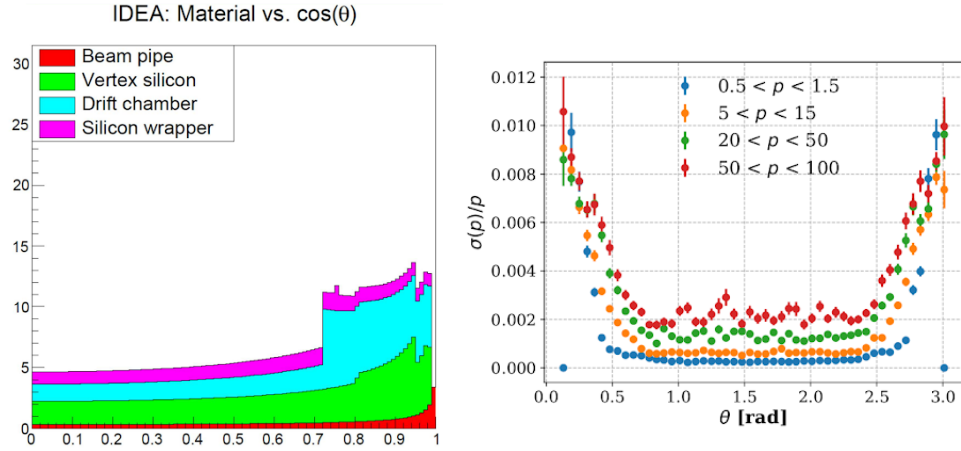


Fig. 15 Left: IDEA material budget versus the cosine of the azimuthal angle θ . Right: muon momentum resolution using the IDEA drift chamber.

¹https://indico.cern.ch/event/1236823/contributions/5210039/attachments/2576345/4442600/2023_01_16_winter2023_Electrons_brems.pdf

3 Event selection

In this section, a basic and a baseline event selection are introduced, in order to focus on regions where the signal process is prominent and effectively suppresses background processes. The main backgrounds in this analysis are WW, ZZ, and Z/ γ , but other rare processes are included as well (see Section 2 for a complete list of samples). Only electrons and muons are used (referred to as leptons), which can be measured with high precision such that tight selection cuts can be applied.

The event selection is divided into two parts: preselection cuts (see Section 3.1), and kinematic cuts (see Section 3.2). An overview of all the selections and the event yields is presented in Section 3.4.

3.1 Preselection cuts

Before applying kinematic cuts to focus on the signal region, a set of preselection cuts is applied to leptons in order to identify whether they are likely originating from the $e^+ + e^- \rightarrow ZH$ process or background processes. The selection for the leptons is as follows:

- **Selection of at least 2 leptons.** Ensure the event contains a minimum of two leptons. The leptons are directly taken from the ReconstructedParticles collection.
- **Requirement of at least one isolated lepton with $I_{\text{rel}} < 0.25$.** Reduce background contributions by requiring that at least one lepton be well-separated from other particles (mainly semi-leptonic flavor decays). For a given lepton, the relative cone isolation I_{rel} is defined as the sum of all the ReconstructedParticles momenta within a cone of radius $\Delta R < 0.5$, divided by the lepton momentum.
- **Momentum threshold $p > 20$ GeV.** Exclude low-energy leptons and minimize noise from soft radiation.
- **Opposite charge requirement.** Ensure that the leptons have opposite charges in order to enhance the signal and suppress background processes.

In case more than two leptons are present in the event, the lepton pair is selected that minimizes the following expression:

$$\chi^2 = 0.6 \times (m_{\ell\ell} - m_Z)^2 + 0.4 \times (m_{\text{rec}} - m_h)^2, \quad (4)$$

with $m_Z = 91.2$ GeV, $m_h = 125$ GeV, $m_{\ell\ell}$ the invariant mass of the lepton pair and m_{rec} the recoil. The fractions 0.6 and 0.4 have been approximately optimized to take into account the different resolutions of the two terms. The χ^2 encapsulates both the kinematic constraints on the Z and Higgs mass and therefore optimally selects the best lepton pair to originate from the radiating Z.

278 3.2 Kinematic cuts

279 An additional set of kinematic cuts is applied to further reduce the background events
280 and enhance signal purity. A set of plots motivating the selection requirements are
281 given in Appendix A. The cuts are only based on the lepton information, to retain the
282 Higgs decay mode independence (see Section 5 for an explicit evaluation of the decay
283 mode independence).

- 284 • **Invariant mass of the di-lepton pair:** $86 \text{ GeV} < m_{\ell\ell} < 96 \text{ GeV}$ (Fig. A1);
- 285 • **Di-lepton momentum:** $20 \text{ GeV} < p_{\ell\ell} < 70 \text{ GeV}$ (Fig. A2);
- 286 • **Recoil mass:** $120 \text{ GeV} < m_{\text{rec}} < 140 \text{ GeV}$ (Fig. A3);

287 Both preselection and kinematic cuts rely solely on the lepton properties.

288 3.3 Basic and Baseline selections

289 The **”basic selection”** is defined as the set of preselection and kinematic cuts defined
290 above. It is used for the model-independent ZH cross-section analysis.

291 For the Higgs mass analysis, an additional cut is applied to further reduce Z/γ events,
292 which typically contain hard ISR photons collinear to the beam and therefore left
293 undetected, resulting in a peaking behavior of the direction of the missing momentum
294 vector towards the forward regions, as can be seen in Fig. A4. The following cut is
295 thus applied:

- 296 • **Cosine of missing momentum:** $|\cos(\theta_{\text{miss}})| < 0.98$ (Fig. A4).

297 The **”baseline selection”** is thus defined as the basic selection complemented with
298 this additional cut. This additional cut cannot be applied to the model-independent
299 cross-section analysis since it is sensitive to Higgs decay mode containing invisible
300 decays (see Section 5).

301 3.4 Event yields and cut flow

302 Event cut-flows, yields, and selection efficiencies for the muon and electron final states
303 are shown in Fig. 16 and Table 3 respectively. It clearly indicates a strong background
304 reduction while retaining the signal events to a good extent. Due to the additional t-
305 channel production of $Z/\gamma \rightarrow e^+e^-$ events, this background is more abundant in the
306 electron final state w.r.t. the muon final state.

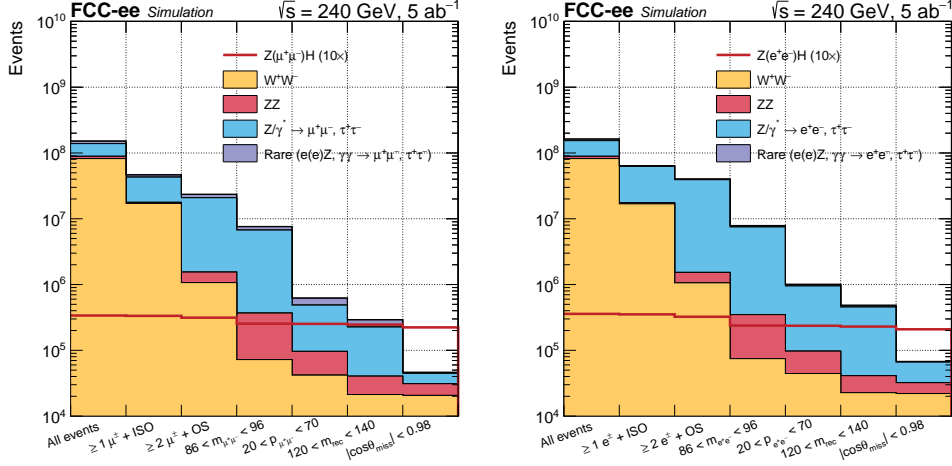


Fig. 16 Event cutflow plots for the muon (left) and electron (right) final states.

307 The recoil distributions after the full event selection are shown in Fig. 17. A narrow
 308 distribution is obtained, as a direct result of the excellent resolution performance of
 309 the IDEA drift chamber. The electron channel is visibly degraded due to the 20% addi-
 310 tional smearing w.r.t. the muons, as explained in Section 2.2. Additionally, the WHIZARD
 311 electron samples contain a small fraction of VBF events which also degrades the res-
 312 olution. Combined with the higher backgrounds, the muon channel will dominate the
 313 uncertainty on the Higgs cross-section and mass.

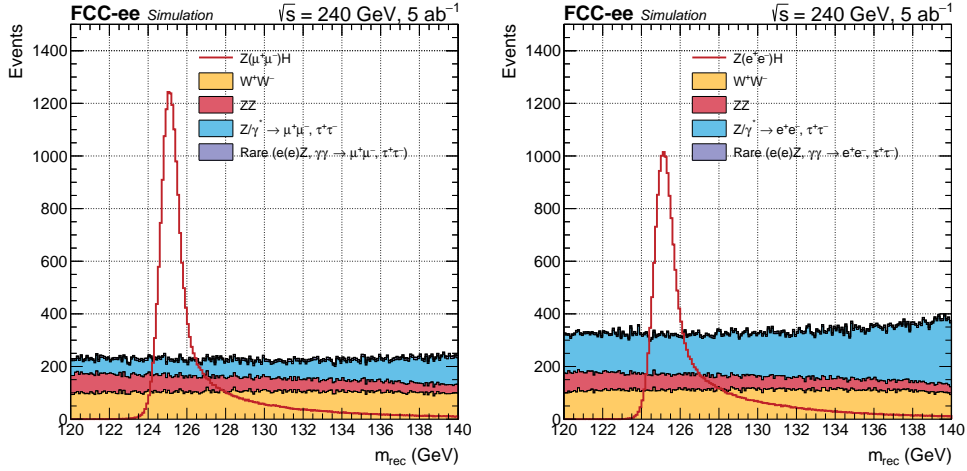


Fig. 17 Recoil distributions after all cuts (including the $\cos(\theta_{\text{miss}})$ cut) for the muon (left) and electron (right) final states.

Table 3 Cut flow and event yields for the muon (top) and electron (bottom) final states. for The error reflects the uncertainty on the Monte Carlo event statistics.

Process	ZH	WW	ZZ	Z/ γ	Rare
Muon final state					
All events	3.38e+04 \pm 3.09e+01	8.22e+07 \pm 4.25e+03	6.79e+06 \pm 9.07e+02	4.98e+07 \pm 4.85e+03	1.31e+07 \pm 1.55e+03
$\geq 1\ell^\pm$ + ISO	3.34e+04 \pm 3.07e+01	1.71e+07 \pm 1.94e+03	6.68e+05 \pm 2.84e+02	2.52e+07 \pm 3.50e+03	3.66e+06 \pm 8.25e+02
$\geq 2\ell^\pm$ + OS	3.14e+04 \pm 2.97e+01	1.07e+06 \pm 4.85e+02	4.77e+05 \pm 2.40e+02	1.93e+07 \pm 3.09e+03	2.61e+06 \pm 6.88e+02
$86 < m_{\ell\ell} < 96$ GeV	2.54e+04 \pm 2.68e+01	7.23e+04 \pm 1.26e+02	2.96e+05 \pm 1.89e+02	6.36e+06 \pm 1.77e+03	8.86e+05 \pm 3.22e+02
$20 < p_{\ell\ell} < 70$ GeV	2.52e+04 \pm 2.67e+01	4.19e+04 \pm 9.61e+01	5.44e+04 \pm 8.12e+01	3.91e+05 \pm 4.39e+02	1.36e+05 \pm 1.58e+02
$120 < m_{\text{rec}} < 140$ GeV	2.46e+04 \pm 2.63e+01	2.13e+04 \pm 6.84e+01	1.92e+04 \pm 4.82e+01	1.85e+05 \pm 3.02e+02	6.61e+04 \pm 1.11e+02
$ \cos(\theta_{\text{miss}}) < 0.98$	2.23e+04 \pm 2.51e+01	2.06e+04 \pm 6.74e+01	1.04e+04 \pm 3.56e+01	1.36e+04 \pm 8.01e+01	1.63e+03 \pm 1.17e+01
Efficiency (%)	6.60E+01	2.51E-02	1.53E-01	2.73E-02	1.24E-02
Electron final state					
All events	3.58e+04 \pm 3.27e+01	8.22e+07 \pm 4.25e+03	6.79e+06 \pm 9.07e+02	6.49e+07 \pm 5.53e+03	9.23e+06 \pm 1.18e+03
$\geq 1\ell^\pm$ + ISO	3.52e+04 \pm 3.24e+01	1.69e+07 \pm 1.93e+03	6.65e+05 \pm 2.84e+02	4.50e+07 \pm 4.66e+03	1.54e+06 \pm 4.60e+02
$\geq 2\ell^\pm$ + OS	3.24e+04 \pm 3.11e+01	1.06e+06 \pm 4.83e+02	4.69e+05 \pm 2.38e+02	3.77e+07 \pm 4.28e+03	1.03e+06 \pm 3.65e+02
$86 < m_{\ell\ell} < 96$ GeV	2.38e+04 \pm 2.66e+01	7.47e+04 \pm 1.28e+02	2.74e+05 \pm 1.82e+02	7.15e+06 \pm 1.86e+03	3.73e+05 \pm 1.59e+02
$20 < p_{\ell\ell} < 70$ GeV	2.36e+04 \pm 2.66e+01	4.44e+04 \pm 9.89e+01	5.28e+04 \pm 7.99e+01	8.54e+05 \pm 6.44e+02	5.56e+04 \pm 8.55e+01
$120 < m_{\text{rec}} < 140$ GeV	2.30e+04 \pm 2.62e+01	2.27e+04 \pm 7.07e+01	1.84e+04 \pm 4.72e+01	4.14e+05 \pm 4.48e+02	2.88e+04 \pm 6.30e+01
$ \cos(\theta_{\text{miss}}) < 0.98$	2.09e+04 \pm 2.50e+01	2.20e+04 \pm 6.96e+01	1.02e+04 \pm 3.51e+01	3.40e+04 \pm 1.28e+02	1.46e+03 \pm 1.11e+01
Efficiency (%)	5.84E+01	2.68E-02	1.50E-01	5.24E-02	1.58E-02

4 Higgs mass measurement

In this section, the Higgs mass analysis is outlined, aiming to estimate a realistic uncertainty with the dominant systematic effects included. The analysis uses $Z(\ell^+\ell^-)H$ events, where $\ell = e$ or μ . Indeed, a precise measurement of the Higgs mass relies on an accurate lepton momentum resolution in order to precisely resolve the recoil mass distribution and infer the mass from it. With the IDEA drift chamber, excellent performances can be obtained for both muon and electrons, as explained in Section 2.2.

The Higgs mass measurement starts with an event selection to reduce the backgrounds while retaining as much as possible the signal events. The baseline event selection is described in Section 3. In order to further enhance the sensitivity on the Higgs mass uncertainty, the events are categorized according to their lepton azimuthal angle, driven by the material differences. The effect on the resolutions and recoil distributions is explained in Section 4.1.

To infer the Higgs mass uncertainty, a maximum likelihood fit is deployed using the RooFit-based CMS Combine tool. For this, two steps are necessary: the analytic modeling of the signal and background shapes, and the dependency of the analytic shapes on the Higgs mass in order to perform the horizontal morphing. Both steps are explained in detail in Section 4.2. Similarly, the background modeling is described in Section 4.3. The analytic models are then used to construct the likelihood, which is minimized to the Asimov dataset in order to extract the uncertainty on the Higgs mass. Results are discussed in Section 4.4, whereas other fit configurations are discussed in Section 4.5.

4.1 Event categorization

Due to the material dependency in the central and forward regions of the detector, the events are classified into three distinct categories, based on whether the azimuthal angle θ of the lepton is central ($0.8 < \theta < 2.34$ rad) or forward (the complementary azimuthal space):

- Central-central (CC): both leptons are in the central region of the detector;
- Central-forward (CF): one lepton is central and the other lepton is forward;
- Forward-Forward (FF): both leptons are in the forward region of the detector.

In the end, a total of 6 categories are used in the final fit: 3 for the muon and 3 for the electron final states. The different recoil distributions for all categories are shown in Fig. 18. All the categories are fitted simultaneously in the final fit to retain the total statistical power of the selected events. The advantage of such categorization is that the different recoil resolutions are separated in the fit, leading to a higher sensitivity to the Higgs mass (see Section 4.4). Another advantage of the categorization is that it eases the parameterization of the signal shapes (see next paragraph) because different resolution components are decoupled.

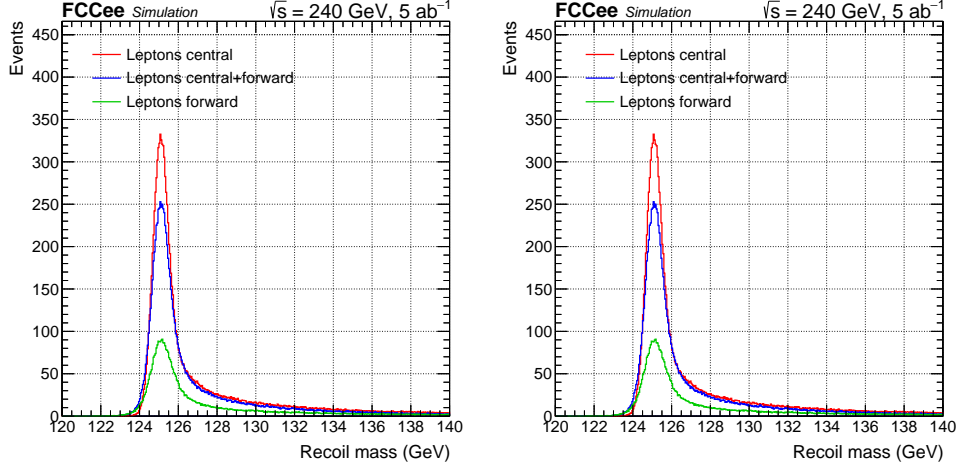


Fig. 18 Categorized recoil distributions for the muon (left) and electron (right) final states.

4.2 Signal modeling

It is important to accurately model analytically the recoil signal shapes in the recoil mass range of $m_{\text{rec}} \in [120, 140]$ GeV. Both the peak and tails are important to capture all possible effects such as lepton resolution, initial state radiation, and beam energy spread. All processes and uncertainties leading to deviations in the distribution should be taken into account as systematic uncertainties.

In the current analysis, the signal shapes have to be modeled for each of the 6 categories. To be complete, also the inclusive muon and electron shapes are considered (i.e. without azimuthal categorization). Throughout this section, the inclusive muon category is used as an example, but the procedure is applied to the other categories. All the fits and plots are given in Appendix B.

Typically, recoil distributions are modeled using a (double) Crystal-Ball function (DSCB). This function has 7 degrees of freedom: the overall normalization, mean, width, and 2 parameters each describing the left and right-hand tails of the distribution. The result after fitting the 125 GeV sample to the DSCB is shown in Figure 19 (left). Both the peak and tails are not well modeled, and this cannot be solved by optimizing the initial fit parameters. Therefore a more appropriate description of the recoil distribution is needed having more degrees of freedom.

After various attempts, a combination of two single-sided (mirrored) Crystal-Ball functions plus a Gaussian was proven to model the signal sufficiently well (2CBG). Both Crystal-Ball functions share the same mean and width, though the offsets and tails are independent. The Gaussian is added to cope with the transition of the peak to the tails, therefore it has a separate mean and width. The total PDF is given by the following equation:

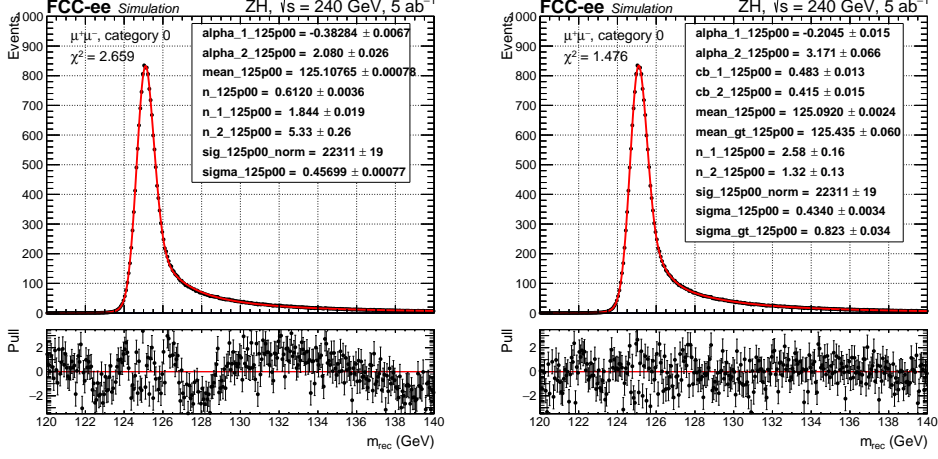


Fig. 19 Signal modeling with DSCB (left) and 2CBG (right).

$$\text{pdf}_{\text{rec}} = cb_1 \text{CB}(\mu, \sigma, \alpha_1, n_1) + cb_2 \text{CB}(\mu, \sigma, \alpha_2, n_2) + \text{Gauss}(\mu_{gt}, \sigma_{gt}) \quad (5)$$

Two coefficients cb_1 and cb_2 regulate the normalization of the Crystall-Ball functions, whereas the normalization of the Gaussian is constrained to the unity normalization of the PDF. However, both Crystal-Ball functions are dominant in normalization ($\approx 85\%$) and the Gaussian term contributes only to $\approx 15\%$. In total, the pdf contains 10 degrees of freedom, sufficient to properly model the signal template, as shown in Fig. 19 (right). In Fig. 20 (left), the decomposition of the 3 terms in the recoil PDF for $m_h = 125$ GeV is shown, clearly indicating the contribution of each term.

In order to know the impact of the Higgs mass on the recoil shape and the parameters of the 2CBG PDF, additional samples around the nominal mass sample of $m_h = 125$ GeV were generated (± 50 MeV and ± 100 MeV). Each mass sample is fitted to the 2CBG PDF and the parameters are extracted (see Appendix B for all plots). No strong biases relative to the statistical uncertainties are observed for all the recoil mass fits.

The 10 fit parameters from the 2CBG PDF are then parameterized as a function of m_h , such that the entire signal model depends only on m_h and the functions used. It was found that only the means (both μ and μ_{gt}) and overall normalization (due to varying cross-section as a function of m_h) do depend significantly on the Higgs mass, whereas the other parameters are nearly constant. This means that the shape is rather independent of the mass (in the vicinity of 125 GeV), but only a linear shift of the mean as a function of m_h . All the 10 parameters, whether constant or not, are interpolated using splines and are shown in Appendix B. As an example, in Fig. 21 (left), the mean (μ) spline as a function of m_h is shown. A good linear dependency is observed.

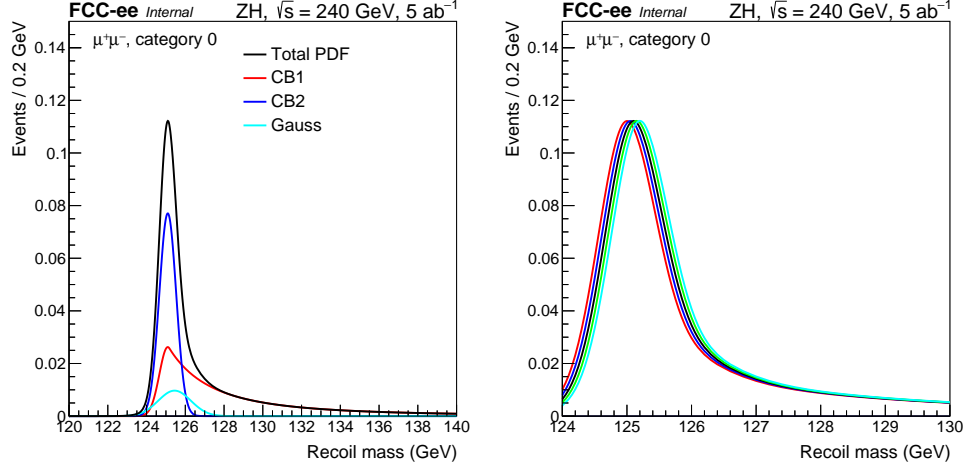


Fig. 20 Decomposition of the 3 terms in the recoil PDF for 125 GeV (left), fitted recoil distributions for different masses around 125 GeV (right).

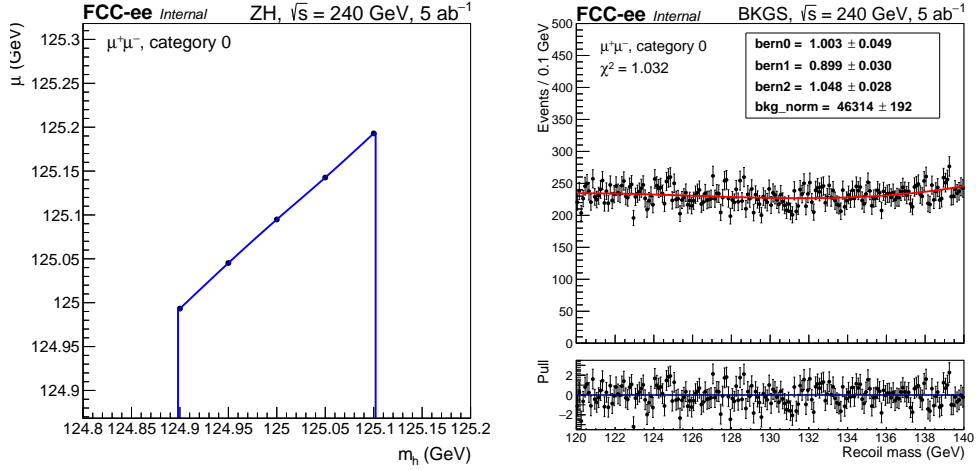


Fig. 21 Left: example spline for the mean; Right: backgrounds modeling using a third-order Bernstein polynomial.

4.3 Background modeling

The modeling of the background is easier due to its smoothly falling behavior in the recoil mass range of $m_{\text{rec}} \in [120, 140]$ GeV. Because there is no constraint power for the individual backgrounds, all the backgrounds are merged together in a single process. The total background is modeled as a third-order polynomial, as shown in Figure 21 (right). Bernstein polynomials have been chosen which are positive-definite in the (re-scaled) range of $[0, 1]$ which enhances the stability during the fit. The three coefficients of the polynomial are kept constant, whereas the total normalization is kept floating.

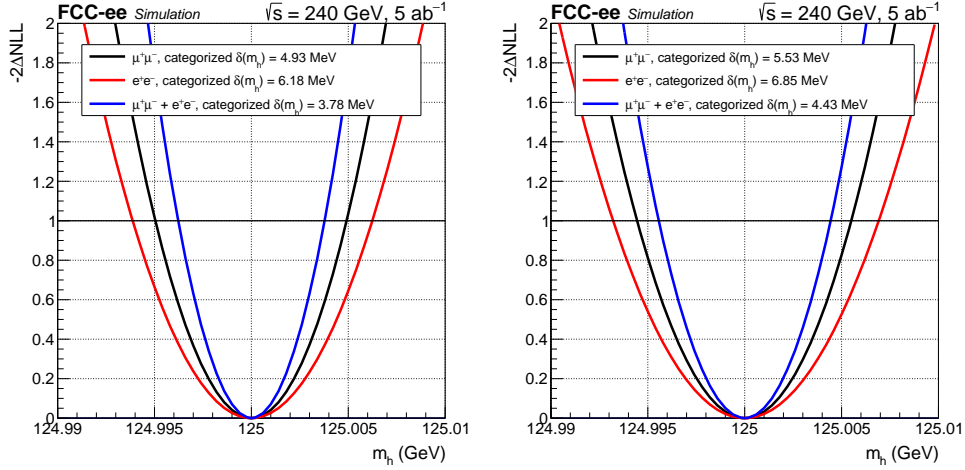


Fig. 22 Likelihood scan statistical-only (left) and statistical+systematics (right).

4.4 Results

Statistical tests and fits are performed using the parameterized signal and background shapes, within the framework of Combine, the CMS statistical framework developed in the context of Higgs analyses. The signal and background analytical shapes are fitted to the pseudo-data Asimov dataset (i.e. randomized per-bin events with a mean equal to the sum of signal+background). As a reference, the 125 GeV signal sample has been chosen to construct the Asimov dataset. During the fit, the Higgs mass m_h and the background normalization are left floating, where the 2CBG is fully parameterized as a function of m_h using splines. A likelihood scan is performed to extract the Higgs mass with robust uncertainties.

Several systematic uncertainties are incorporated in the fit. An overview and discussion of the systematic sources are given in Section 6 (the nuisances are shared with the cross-section analysis). They all affect the shape of the recoil distribution and therefore the alternative shapes also need to be parameterized using the 2CBG as PDF. Such shape variations are incorporated in the Likelihood using a strength parameter ξ , where $\xi = \pm 1$ means the Up/Down variations and $\xi = 0$ the nominal value (there is one parameter per nuisance). This floating parameter enters the likelihood as a multiplicative Gaussian term. They act only on the signal parameters describing the 2CBG and were derived only for the 125 GeV signal sample. It is assumed their magnitude is equal for all the mass points around the vicinity of 125 GeV. The backgrounds are not taken into account by these nuisances, as it is assumed they only act on the normalization with a negligible shape effect. Therefore their potential normalization is absorbed by the overall background normalization. This can change when including control regions to constrain certain nuisances, but this is out of the scope of this study.

A likelihood scan is performed for the simultaneous fit, combining the 3 muon and 3 electron channels. The results are shown in Fig. 22. On the left plot, the statistical-only

uncertainty scans are shown (without systematics). A combined result of 3.78 MeV is obtained at 68 % confidence level. The result is driven by the muon channel; the electron channel improves the result by 25 %. On the right plot, the statistics+systematic likelihood scans are shown. A total uncertainty of 4.43 MeV is obtained at 68 %. Compared to the statistical-only result, the systematics degrade the result by 10 %, therefore the Higgs mass analysis is statistically dominated.

A breakdown of the nuisances and their impact is shown in Figure 23 (left). The dominant uncertainty is the center-of-mass energy, which is estimated to be 2 MeV and directly scales the uncertainty on the mass (see Section 6.3). The other nuisances impact the analysis with less than 1 MeV, in agreement with the back-of-the-envelope calculations shown in Section 6.

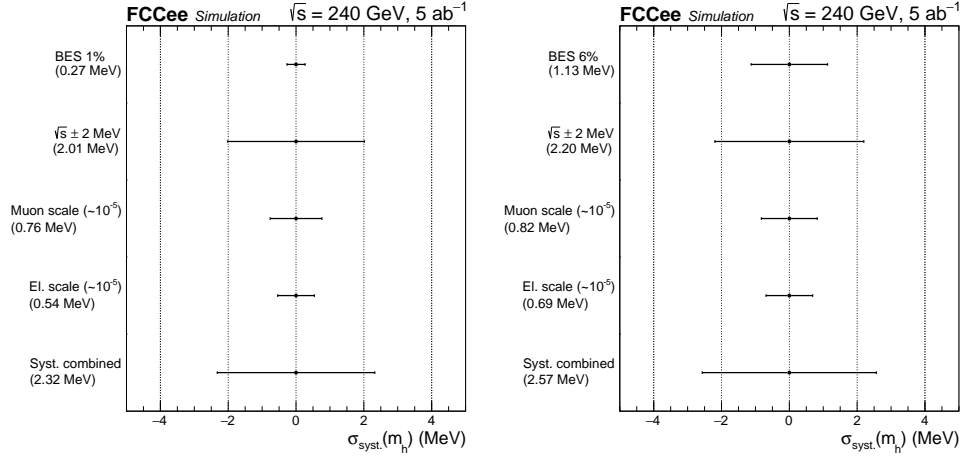


Fig. 23 Uncertainty breakdown on the mass analysis for the nominal fit with BES 1 % (left) and BES 6 % (right). The slight differences in impact for the other nuisances are due to the correlations between them.

4.5 Auxiliary fits

Several auxiliary fits in different configurations have been performed to check dependencies and impacts. The studies and results are performed on the inclusive muon category and are reported as relative to the standard fit (statistical only) unless stated otherwise. A list is given below:

1. **Inclusive fits:** Instead of categorizing the events in 3 (or 6) azimuthal categories, the fit is performed in a single category for the muon and electron final states. The uncertainty on the mass degrades by 15–20 % (see Fig. 24 for the likelihood scans).
2. **Degrading electron resolution:** The current modified IDEA detector with a crystal calorimeter is very optimistic, whereas the default IDEA design relies on the Dual Readout calorimetry. The lack of crystals strongly reduces the electron resolution performance. To assess such degradation, the electron resolution was smeared twice as much as the muons (instead of 1.25 using crystals). The electron-only sensitivity got reduced by a factor of 15 % (from 6.18 MeV to 7.19 MeV, stat. only), whereas the total statistical uncertainty (with muons combined) got reduced with a factor of 5 % (from 3.78 MeV to 4.0 MeV). The relative gain from the electrons reduces from 25 % to 20 % (see Fig. 25 (right)).
3. **Magnetic field:** The magnetic field was increased from 2 to 3 Tesla, leading to a better momentum resolution (the resolution scales approximately with $\propto 1/B$). The uncertainty on the Higgs mass improved by 15 %. The rather limited improvement is due to the beam energy spread, which degrades the recoil distribution.
4. **Silicon tracker:** The drift chamber is replaced by a full silicon tracker. Due to the enhanced multiple scattering (more material), the resolution is expected to degrade, especially for low-momentum leptons (the resolution scales approximately with $\propto 1/\sqrt{X_0}$). Indeed, the uncertainty on the Higgs mass increased by 35 %.
5. **Increased BES uncertainty:** In the nominal case, the BES is estimated to be accurate up to 1 %, based on radiative return events (see Section 6.1). An accuracy of 6 % is obtained from the accelerator bunch length monitoring only. This 6 % BES uncertainty was evaluated on the Higgs mass and it degraded the uncertainty with 3 %. The resulting impacts are shown in Fig. 23 (right), where the absolute impact on the BES increased from 0.27 MeV to 1.13 MeV.
6. **Switching off BES:** The beam energy spread of 0.185 % strongly contributes to the broadening of the recoil distribution. The effect has been studied by switching off entirely the beam energy spread in the analysis. Based on statistical-only studies, the improvement in the Higgs mass uncertainty is about 50 %.
7. **Ideal resolution:** After the event selection, the reconstructed muon kinematics is replaced by the generator-level kinematics, to mimic the ideal resolution (but realistic backgrounds and event selection). The improvement in the Higgs mass was found to be 30 %.
8. **Freeze backgrounds:** Freezing the normalization of the background does not change the uncertainty on the Higgs mass, as both shapes are very distinct and operate orthogonally (the mass moves horizontally whereas the background normalization moves vertically).

489 **9. Remove backgrounds:** The effect on the backgrounds was evaluated by running
 490 the fit without backgrounds. For the combined fit, statistical only, the uncertainty
 491 on the Higgs mass is improved from 3.78 MeV to 2.99 MeV, i.e. a relative
 492 improvement of 25 % (see Fig. 25 (left)).

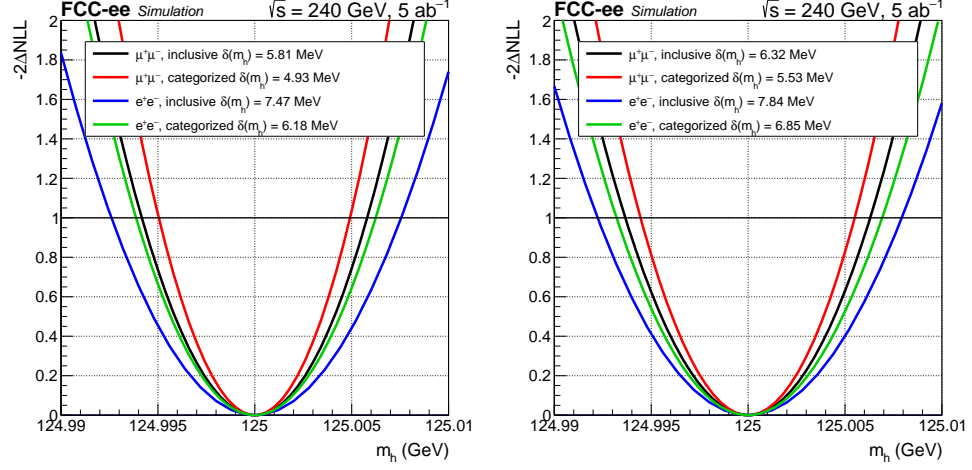


Fig. 24 Likelihood scan statistical-only (left) and statistical+systematics (right), by comparing the categorized and inclusive fits.

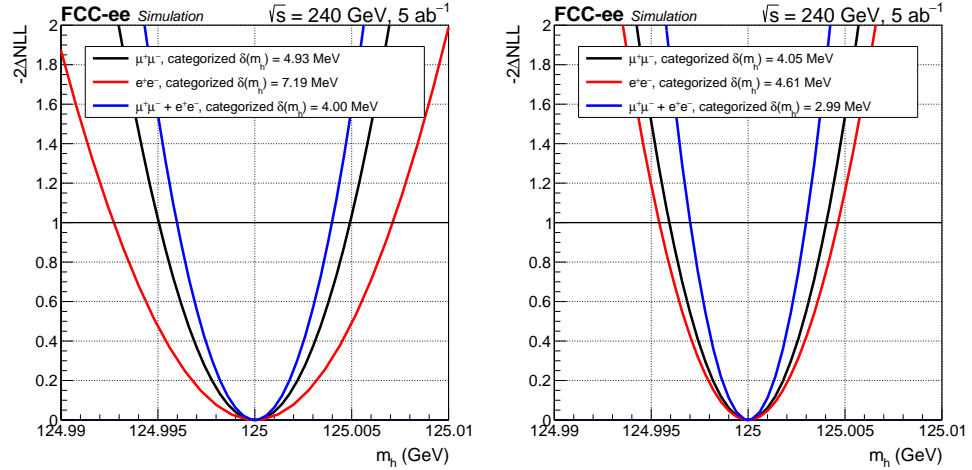


Fig. 25 Statistical-only likelihood scans when reducing the electron resolution with a factor of 2 w.r.t the muons (left) and the nominal fit but removing the backgrounds (right).

5 ZH cross-section measurement

Unlike the mass measurement in Section 4, where strict selections can be applied to increase the signal significance, in the cross-section measurement model independence of the Higgs decay modes must be maintained.

The recoil mass technique, as detailed in Section 1.2, provides a unique opportunity to measure the cross-section of the $e^+ + e^- \rightarrow ZH$ production mode in a Higgs decay model-independent manner. Thus, any deviation from the Standard Model prediction would indicate the presence of new physics.

During the mass measurement, we applied the selection $|\cos(\theta_{\text{miss}})| < 0.98$ to reduce the $Z \rightarrow \ell^+ \ell^-$ events. However, this selection introduces a bias towards Higgs decays involving neutrinos (or any non-Standard Model invisible decays) which induce intrinsic missing momentum, causing these events to be rejected.

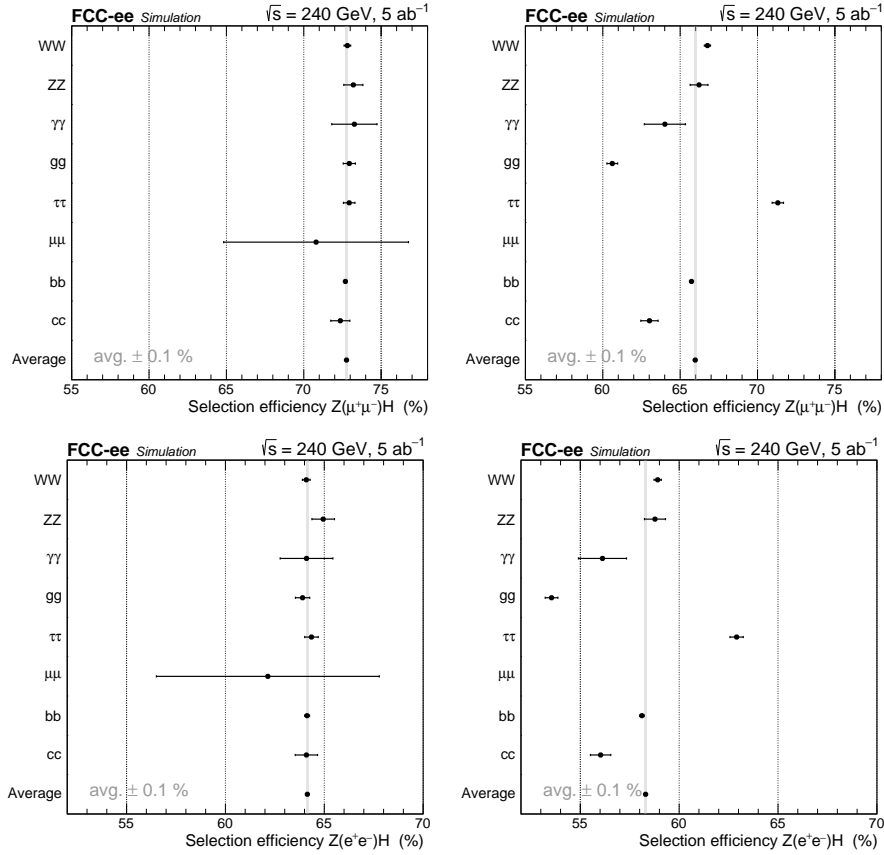


Fig. 26 Selection efficiency of the different Higgs decay modes with $Z \rightarrow \mu^+ \mu^-$ (top row) and $Z \rightarrow e^+ e^-$ decay mode (bottom row). The left column shows the selection efficiency with the basic selection (without $\cos(\theta_{\text{miss}})$ cut), and the right column shows selection efficiency with baseline selection (with $\cos(\theta_{\text{miss}})$ cut).

505 The selection efficiency of the various Higgs decay modes for $Z \rightarrow \mu^+\mu^-$ (top) and
 506 $Z \rightarrow e^+e^-$ decay mode is examined in Figure 26. The left plots delineate the selection
 507 efficiency applying basic selection criteria, excluding the $\cos(\theta_{\text{miss}})$ cut. In contrast, the
 508 plots on the right exhibit the selection efficiency when the baseline selection criteria
 509 are employed, inclusive of the $\cos(\theta_{\text{miss}})$ cut, clearly indicating a violating of the Higgs
 510 decay mode independency.

511 In the $e^+ + e^- \rightarrow \text{ZH}$ cross-section measurement, after applying the basic selec-
 512 tion criteria detailed in Section 3, we do not use the $\cos(\theta_{\text{miss}})$ cut and replace it
 513 with a Boosted Decision Tree (BDT) approach to further reject the background. This
 514 alternative method provides a more accurate representation of the Higgs decay pro-
 515 cesses involving neutrinos while preserving model independence in the cross-section
 516 measurement.

517 5.1 Boosted Decision Tree

518 The Boosted Decision Tree (BDT) is a machine-learning algorithm that has been
 519 widely used in high-energy physics since its introduction in 2005 [17]. As a supervised
 520 learning algorithm, BDT combines the strengths of decision trees with the boost-
 521 ing technique, enhancing the performance and accuracy of the model. **XGBoost** [18]
 522 package is employed to perform the BDT study in this work.

523 5.1.1 Training samples

524 A distinct dataset, which is orthogonal to the dataset presented in Table 2, has
 525 been specifically generated for the purpose of BDT training and validation. This
 526 approach is designed to ensure minimal bias and enhance the model's generalization
 527 capabilities.

528 In the case of the $\mu^+\mu^-$ (e^+e^-) channel, all signal events that meet the basic selection
 529 criteria, without $\cos(\theta_{\text{miss}})$ cut, are utilized for the training process. To maintain a
 530 balanced training and validation set, the total number of background training samples
 531 is set to match the total number of signal samples. Within the various background
 532 processes, the number of events allocated for training is determined based on a propor-
 533 tionality factor, which is the product of each process's cross-section and cut efficiency.
 534 By adhering to this proportional distribution, the training set can better represent the
 535 underlying characteristics of the different processes.

536 The training samples are equally separated into training and validation datasets, where
 537 the training dataset is used to train the BDT model while the validation dataset is
 538 used to verify the performance and generalization of the BDT model, which ensures an
 539 unbiased evaluation of the BDT model's performance and robustness. This partitioning
 540 strategy prevents over-fitting and allows for a more accurate estimation of the model's
 541 performance on unseen data.

542 The specific breakdown of signal and background events for both the $\mu^+\mu^-$ and e^+e^-
 543 channels is documented in Table 4 and Table 5 respectively. Employing this training
 544 strategy, along with the equal separation of training and testing datasets, the BDT

model can achieve a more accurate and robust performance, ultimately contributing to a more reliable analysis in the context of this paper.

Table 4 Training Samples for muon channel. They are all produced at a center-of-mass energy of 240 GeV.

Sample Name	Process	Generator	Training + Validation	cross-section (pb)
Higgs Processes				
wzp6_ee_mumuH	$e^+e^- \rightarrow \mu^+\mu^-H$	WHIZARD + PYTHIA6	873007	0.0067643
Diboson Processes				
p8_ee_ZZ	$e^+e^- \rightarrow ZZ$	PYTHIA8	59261	1.35899
p8_ee_WW_mumu	$e^+e^- \rightarrow WW \rightarrow \mu^+\nu_\mu\mu^-\bar{\nu}_\mu$	PYTHIA8	62966	0.25792
Dilepton Processes				
wzp6_ee_mumu	$e^+e^- \rightarrow \mu^+\mu^-$	WHIZARD + PYTHIA6	551655	5.288
Electron Photon Processes				
wzp6_egamma_eZ_Zmumu	$e^-\gamma \rightarrow e^-Z(\mu^+\mu^-)$	WHIZARD + PYTHIA6	28662	0.10368
wzp6_gammaae_eZ_Zmumu	$e^+\gamma \rightarrow e^+Z(\mu^+\mu^-)$	WHIZARD + PYTHIA6	28512	0.10368
Photon Photon Processes				
wzp6_gaga_mumu_60	$\gamma\gamma \rightarrow \mu^+\mu^-$	WHIZARD + PYTHIA6	141949	1.5523

Table 5 Training Samples for electron channel. They are all produced at a center-of-mass energy of 240 GeV.

Sample Name	Process	Generator	Training + Validation	cross-section (pb)
Higgs Processes				
wzp6_ee_eeH	$e^+e^- \rightarrow e^+e^-H$	WHIZARD + PYTHIA6	769907	0.0067643
Diboson Processes				
p8_ee_ZZ	$e^+e^- \rightarrow ZZ$	PYTHIA8	29894	1.35899
p8_ee_WW_ee	$e^+e^- \rightarrow WW \rightarrow e^+\nu_e e^-\bar{\nu}_e$	PYTHIA8	34874	0.25792
Dilepton Processes				
wzp6_ee_ee_Mee_30_150	$e^+e^- \rightarrow e^+e^-$ (30-150 GeV)	WHIZARD + PYTHIA6	660832	8.305
Electron Photon Processes				
wzp6_egamma_eZ_Zee	$e^-\gamma \rightarrow e^-Z(e^+e^-)$	WHIZARD + PYTHIA6	7883	0.05198
wzp6_gammaae_eZ_Zee	$e^+\gamma \rightarrow e^+Z(e^+e^-)$	WHIZARD + PYTHIA6	7887	0.05198
Photon Photon Processes				
wzp6_gaga_ee_60	$\gamma\gamma \rightarrow e^+e^-$	WHIZARD + PYTHIA6	28534	0.873

5.1.2 Input variables

In this study, a variety of input variables were selected for the Boosted Decision Tree (BDT) training, with a primary focus on lepton-related variables. Given that the fundamental selection criteria require the presence of a minimum of two leptons, information pertaining to both leptons was incorporated into the BDT training process. In addition to these lepton-related variables, Higgsstrahlung-related and polarization-related variables can also be considered for inclusion in the BDT training to further improve the classification performance, but they are not applied in this paper.

555 To maintain consistency between the $\mu^+\mu^-$ and e^+e^- channels, the same set of
 556 variables was applied to both channels. The BDT input variables, along with their
 557 descriptions, are listed in Table 6. Plots of the input distributions are given in
 558 Appendix C.

Table 6 Input variables for BDT training. The leading or sub-leading lepton is sorted by the lepton momentum.

Variable	Description
$p_{\ell+\ell-}$	Lepton pair momentum
$\theta_{\ell+\ell-}$	Lepton pair polar angle
$m_{\ell+\ell-}$	Lepton pair invariant mass
$p_{l_{\text{leading}}}$	Momentum of the leading lepton
$\theta_{l_{\text{leading}}}$	Polar angle of the leading lepton
$p_{l_{\text{subleading}}}$	Momentum of the subleading lepton
$\theta_{l_{\text{subleading}}}$	Polar angle of the subleading lepton
$\Delta\phi_{\ell+\ell-}$	Acoplanarity of the lepton pair
$\Delta\theta_{\ell+\ell-}$	Acolinearity of the lepton pair

559 The variables under consideration can be classified into three categories. The first
 560 category consists of $p_{\ell+\ell-}$, $\theta_{\ell+\ell-}$, and $m_{\ell+\ell-}$, which encapsulate the information per-
 561 taining to the lepton pair cluster. The second category is composed of $p_{l_{\text{leading}}}$, $\theta_{l_{\text{leading}}}$,
 562 $p_{l_{\text{subleading}}}$, and $\theta_{l_{\text{subleading}}}$, each of which contributes to the understanding of individ-
 563 ual leptonic attributes. The third and final category is represented by $\Delta\phi_{\ell+\ell-}$ and
 564 $\Delta\theta_{\ell+\ell-}$, which elucidate the spatial relationship between the two leptons.

565 These variables serve as input features for the BDT, assisting the algorithm in
 566 distinguishing between signal and background events in both the $\mu^+\mu^-$ and e^+e^-
 567 channels. With these variables, the BDT is able to achieve a high level of classification
 568 performance, improving the overall sensitivity of the analysis.

5.1.3 Hyper-parameters

570 Hyper-parameters serve a crucial role in the configuration of the BDT model.

571 The specific values of the hyper-parameters utilized for the BDT model in this study
 572 are listed in Table 7. The hyper-parameters not explicitly defined here are assigned
 573 their default values in the XGBoost framework.

574 It is important to note that the nomenclature of these hyper-parameters is con-
 575 textual and specific to XGBoost. Thus, their denotation might vary in other BDT
 576 applications.

5.1.4 BDT Performance

578 The results from the BDT training are presented in this section. The performance of
 579 the BDT model is demonstrated by the distribution of BDT scores, feature importance

Table 7 Values of the Hyper-parameters utilized for the BDT model training.

Parameter	Value
n_estimators	350
learning_rate	0.20
max_depth	3
subsample	0.5
gamma	3
min_child_weight	10
max_delta_step	0
colsample_bytree	0.5

of input variables, efficiency, and various performance metrics, including the ROC curve, area under the curve (AUC), error curve, and log loss curve.

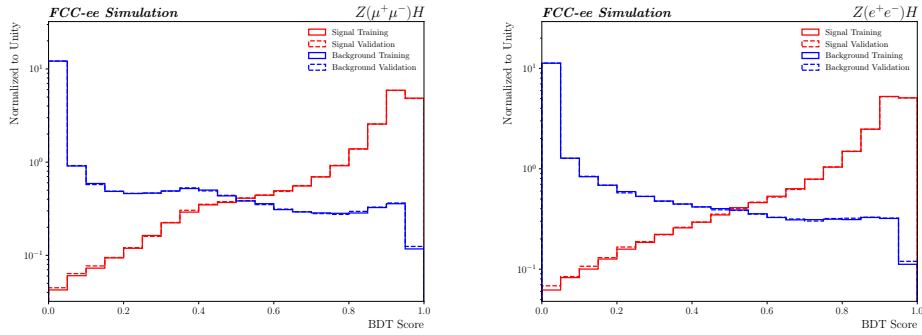


Fig. 27 BDT distributions for $\mu^+\mu^-$ (left) and e^+e^- (right) channel signal and background events from the training (solid) and test (dashed). The BDT model demonstrates consistent performance for both channels, as signal events are predominantly found in regions with high BDT scores, while background events are concentrated at low BDT scores.

Figure 27 shows the BDT score distributions for the $\mu^+\mu^-$ and e^+e^- channels, comparing the signal and background events from the training and validation datasets. The BDT model exhibits consistent performance for both channels, with signal events predominantly located in regions with high BDT scores and background events concentrated at lower BDT scores.

Figure 28 presents the BDT efficiency curves for both $\mu^+\mu^-$ (left) and e^+e^- (right) channels. The curves illustrate the discrimination power of the BDT model, with the signal events showing higher efficiency compared to background events. This representation highlights the effectiveness of the BDT model in separating the signal and background. The relative importance of input variables for the $\mu^+\mu^-$ and e^+e^- channels is displayed in Figure 29. This representation highlights the contribution of each variable in the decision-making process of the BDT model.

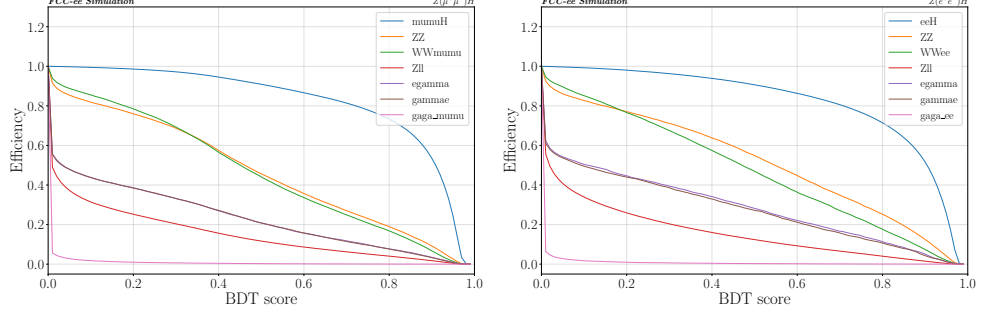


Fig. 28 BDT efficiency curve for $\mu^+\mu^-$ (left) and e^+e^- (right).

Figure 30 shows the ROC curves for the $\mu^+\mu^-$ (left) and e^+e^- (right) channels. The x-axis represents the false positive rate (FPR), and the y-axis represents the true positive rate (TPR). Performance metrics such as the AUC (Figure 31), error curve (Figure 32), log loss curve (Figure 33), further illustrates the effectiveness of the BDT model for both the $\mu^+\mu^-$ and e^+e^- channels.

The good agreements between the curves of the training and validation dataset in all these BDT performance plots reveal the model's ability to discriminate between signal and background events effectively, providing a comprehensive understanding of its generality.

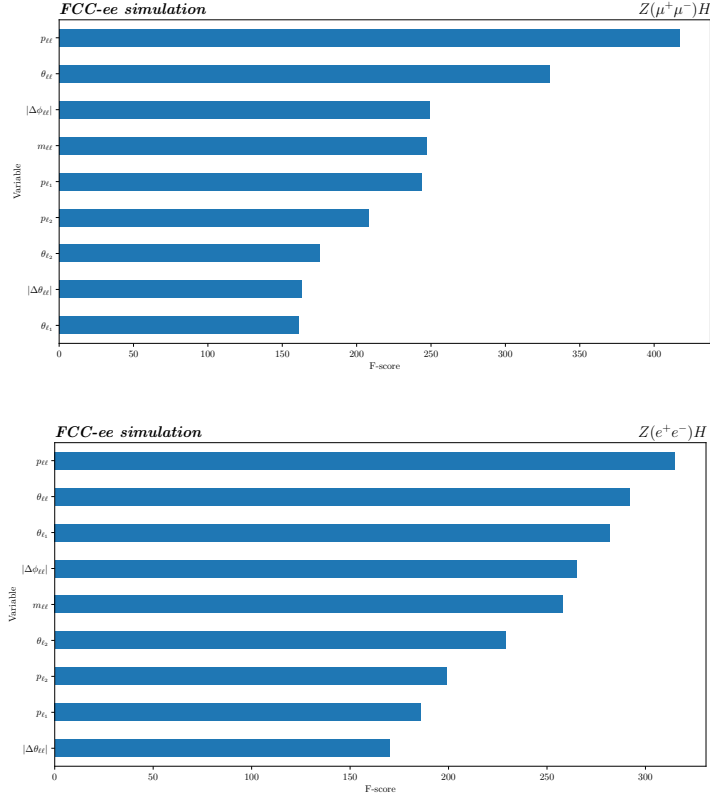


Fig. 29 Feature importance of the input variables for $\mu^+\mu^-$ (top) and e^+e^- (bottom).

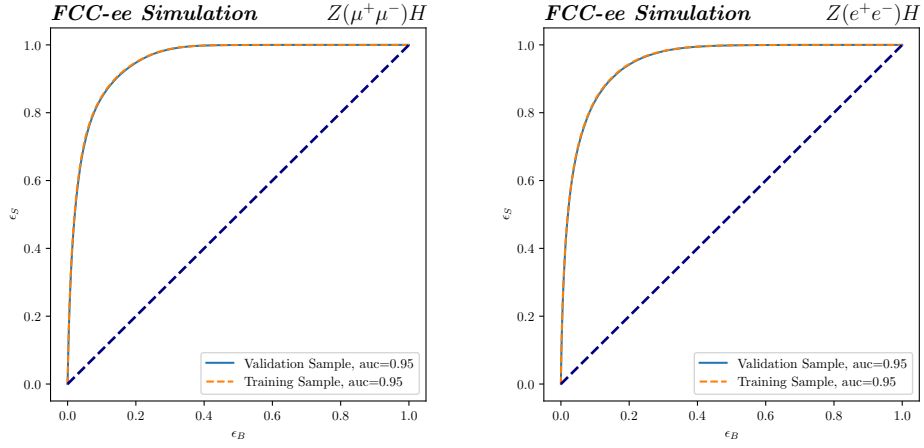


Fig. 30 ROC curve for $\mu^+\mu^-$ (left) and e^+e^- (right).

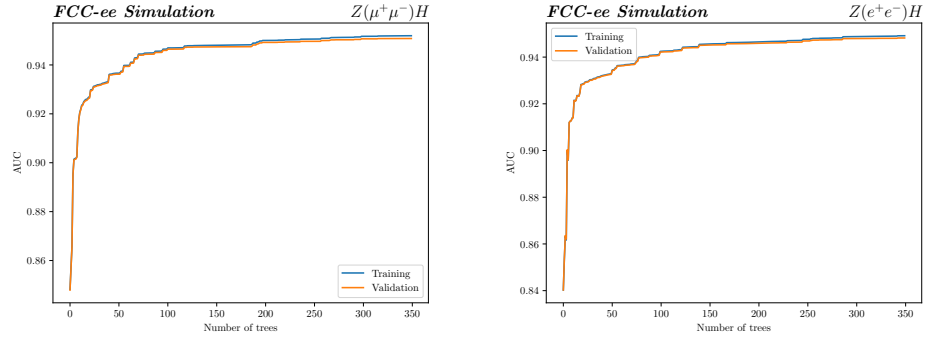


Fig. 31 Area under the ROC curve (AUC) for $\mu^+\mu^-$ (left) and e^+e^- (right).

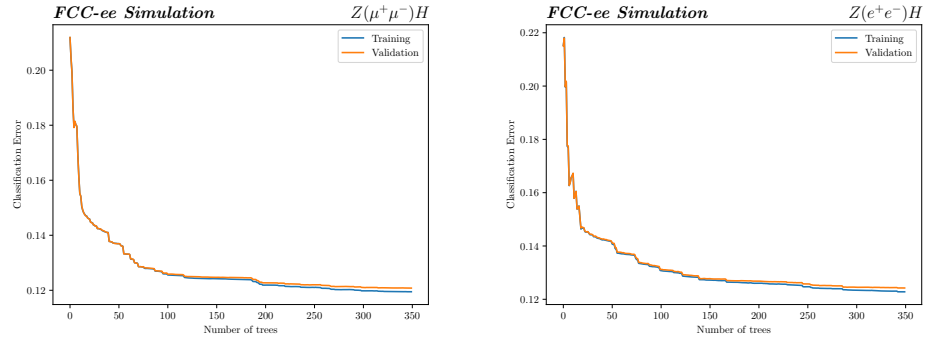


Fig. 32 Classification error curves for $\mu^+\mu^-$ (left) and e^+e^- (right).

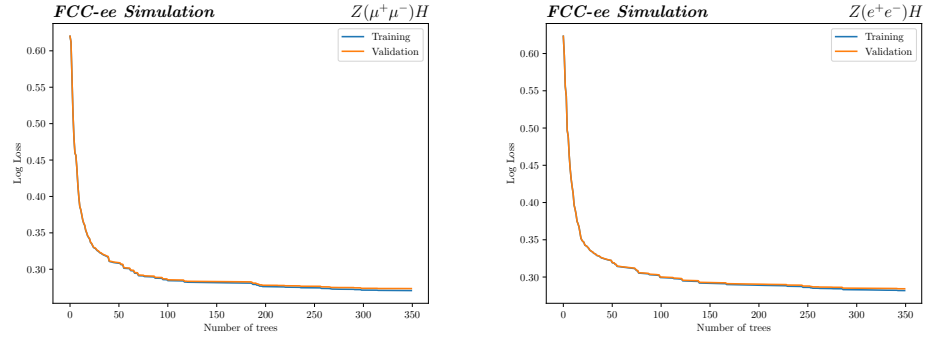


Fig. 33 Log loss curve for $\mu^+\mu^-$ (left) and e^+e^- (right).

5.2 Fitting strategy

The m_{rec} distribution is first used as the fitted shape to extract the signal yield, the same as the mass measurement in Section 4 but with a template fit (binned instead of parametric). After applying the BDT cut on the score > 0.3 , the background shape is distorted, which introduces uncertainties on the background shape, as shown in Figure 34.

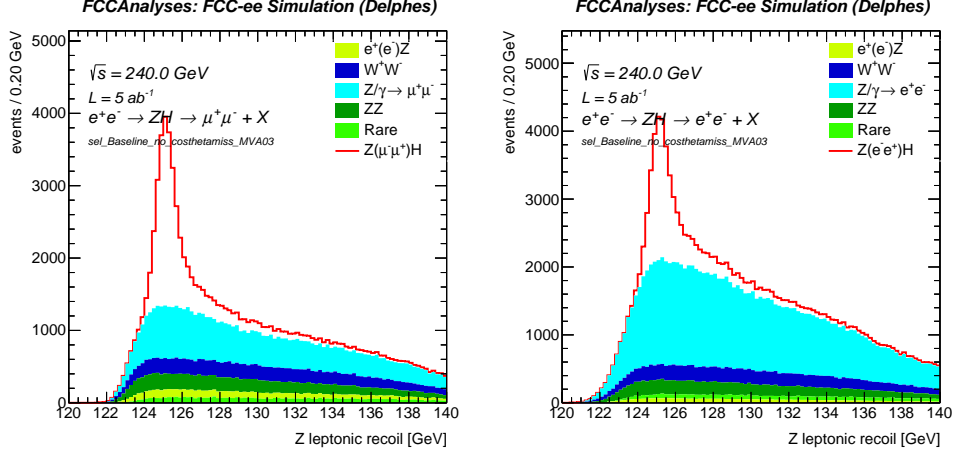


Fig. 34 m_{rec} distribution for the $\mu^+\mu^-$ (left) and e^+e^- (right) channels in linear scale with basic selection, BDT score > 0.3 is applied, i.e. without the $\cos(\theta_{\text{miss}})$ cut.

For the cross-section measurement, the signal yield is the only parameter of interest, thus the precise distribution of the signal shape is not required. Therefore, the binned fit method is introduced to avoid bias on the shapes. The model-independent after BDT cuts are also verified, but this prevents us to use a more powerful BDT model. With more powerful input variables used in the training, the BDT cut will be more powerful but potentially break the model-independent requirement.

In Section 5.2.2, the BDT score shape is introduced as the fitted shape can avoid applying the BDT cuts, thus the model-independent requirement is always satisfied (due to the basic selection that was proven already to be model-independent).

A binned fit method was employed utilizing the m_{rec} in Section 5.2.1 or BDT response distribution in Section 5.2.2.

5.2.1 Fit on recoil mass distribution

The m_{rec} distribution is first used as the fitted shape to extract the signal yield, the same as the mass measurement in Section 4.

Figure 35 displays the m_{rec} distributions for the $\mu^+\mu^-$ and e^+e^- channels with basic selection. Figure 36 shows the m_{rec} distributions for the $\mu^+\mu^-$ and e^+e^- channels with baseline selection, i.e. basic selection with the additional $\cos(\theta_{\text{miss}})$ cut.

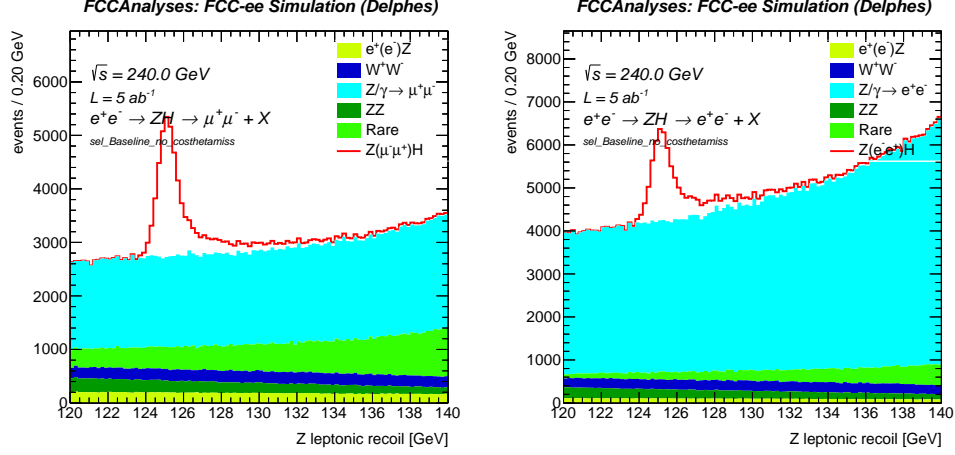


Fig. 35 m_{rec} distribution for the $\mu^+\mu^-$ (left) and e^+e^- (right) channels in linear scale with basic selection, i.e. without the $\cos\theta_{\text{missing}}$ cut.

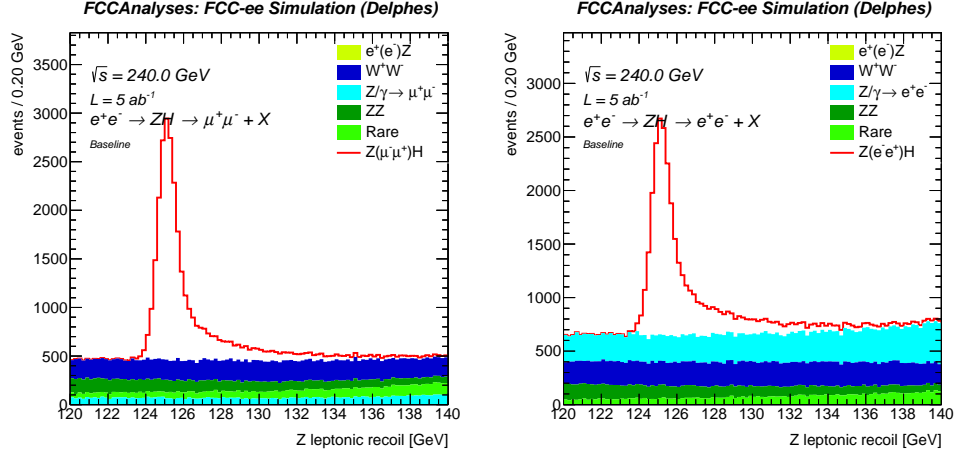


Fig. 36 m_{rec} distribution for the $\mu^+\mu^-$ (Left) and e^+e^- (Right) channels in linear scale with baseline selection, i.e. with the $\cos\theta_{\text{missing}}$ cut.

626 The binned fit is applied on the m_{rec} distribution on both the baseline selection and
 627 baseline without $\cos(\theta_{\text{miss}})$ cut.

628 The log-likelihood scans on baseline shape are depicted in Figure 37 (left). Fitting the
 629 baseline selection results in 0.97 % and 1.15 % uncertainty on the cross-section for
 630 $\mu^+\mu^-$ and e^+e^- respectively. The $\mu^+\mu^-$ and e^+e^- combined fit lower the uncertainty
 631 down to 0.74 %. The $\mu^+\mu^-$ channel is the dominant channel while e^+e^- improves the
 632 uncertainty by 24 %.

633 Removing the $\cos(\theta_{\text{miss}})$ cut ensures model-independency but increases the cross-
 634 section uncertainty, from 0.74 % to 1.19 % (i.e. by 61 %), for the $\mu^+\mu^-$ plus e^+e^-

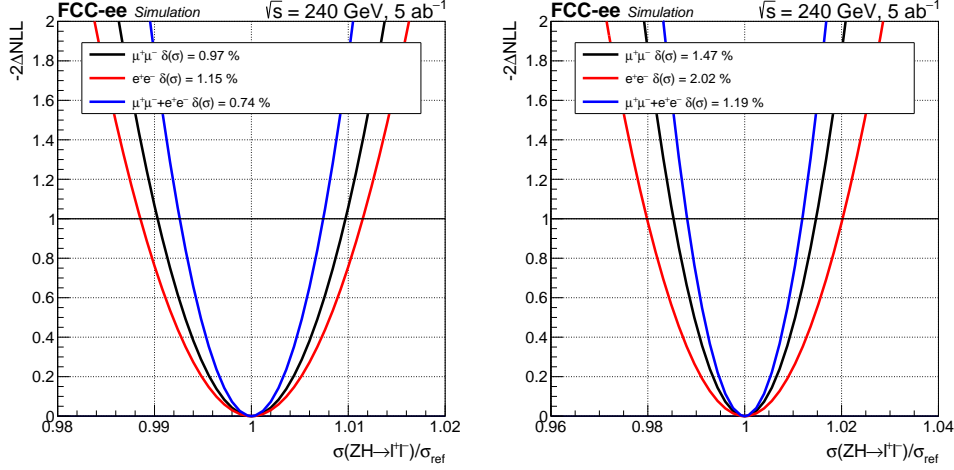


Fig. 37 Comparison of log-likelihood fit results: the left panel shows the fit results using m_{rec} as the input parameter, while the right panel presents the fit results obtained without the $\cos(\theta_{\text{miss}})$ cut. The differences in the fit profiles illustrate the impact of including or excluding the $\cos(\theta_{\text{miss}})$ cut on the fitting process.

channel combined result. The individual results are 1.47 % and 2.02 %, for the $\mu^+\mu^-$ and e^+e^- channels respectively.

5.2.2 Fit on BDT score distribution

Since the cross-section is only related to the signal yield, it can be extracted by fitting on any variable. After training the BDT model, the BDT score became the most powerful variable to separate signal and background events. Therefore, the BDT score distribution is the best candidate for fitting among all the variables.

Figure 38 shows the BDT score distributions for both the $\mu^+\mu^-$ (left) and e^+e^- (right) channels in a logarithmic scale, after basic selection, highlighting the signal and background shapes used in the template fit. The events in these plots are normalized by the luminosity (5 ab^{-1}) and cross-section, which enables a direct comparison of the different distributions. In both panels, the signal events are represented by a red line, while the background events are shown as a stacked histogram.

The main purpose of these plots is to illustrate the distinct shapes of the signal and background distributions, which are crucial for the binned fitting procedure. The normalization by luminosity and cross-section ensures that the distributions are presented on a scale that reflects the events that could be collected in the detector, enabling the comparison of their shapes and the assessment of the binned fitting procedure's performance.

Furthermore, the overlaid fitting templates, which are the expected distributions used in the fitting process, demonstrate a good agreement with the actual BDT score distributions. This confirms that the template fitting procedure is reliable and can effectively capture the features of the signal and background events.

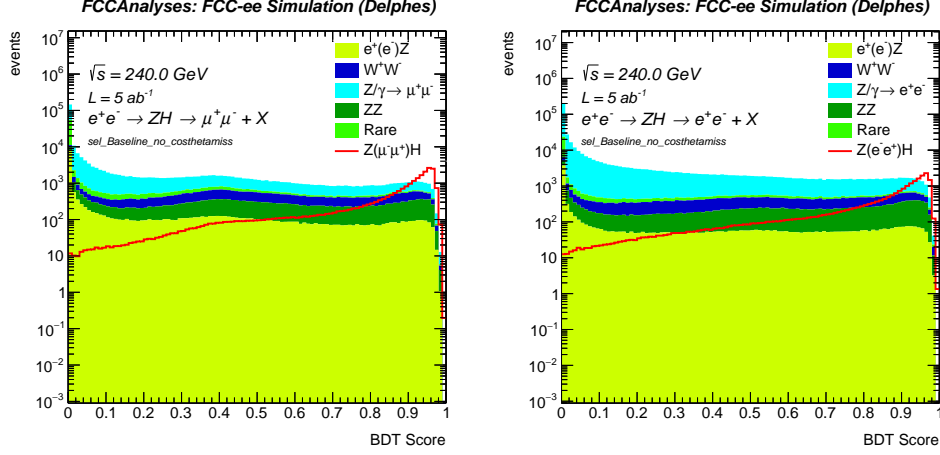


Fig. 38 BDT score distributions and fitting templates for the $\mu^+\mu^-$ (left) and e^+e^- (right) channels in log scale. The distributions demonstrate the BDT model's ability to effectively differentiate signal and background events, while the overlaid templates represent the expected distributions used in the fitting process.

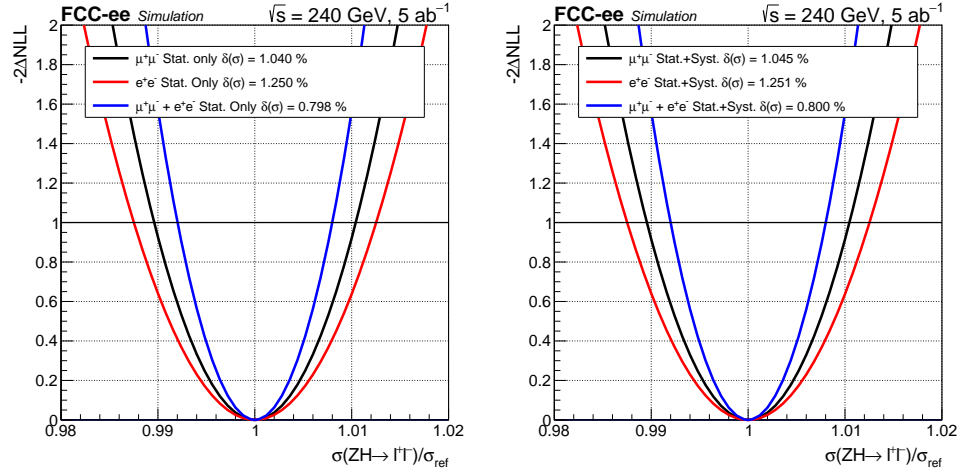


Fig. 39 Log-likelihood fit results using the BDT score as the input parameter. The fit profile demonstrates the differences in the fitting process when employing an alternative input parameter. The left plot shows the fit results only considering statistical uncertainty while the right plot includes the BES 1 %, center-of-mass, lepton momentum scale as systematic uncertainties.

When fitting on the BDT score with the basic selection, the uncertainty for the $\mu^+\mu^-$ channel is 1.05 % and 1.27 % for the e^+e^- channel, while the combined uncertainty becomes 0.80 % (see Fig. 39). The $\mu^+\mu^-$ is here also the leading channel and e^+e^- improves the uncertainty by 23 %.

By employing the binned fit method using the BDT score, the analysis gains enhanced sensitivity and precision in estimating the signal yields for the $\mu^+\mu^-$ and e^+e^-

channels in a model-independent way and have a sensitivity comparable to the model-dependent analysis which uses the $\cos(\theta_{\text{miss}})$ cut (0.80 % vs. 0.74 %). Including the BES 1 %, center-of-mass, lepton momentum scale as systematic uncertainties increase the combined uncertainty to 0.800 % (0.798 % for statistical only). The BES is the leading systematic uncertainty which has about 0.07 % impact on the results. Center-of-mass, muon scale, and lepton scale are negligible (see Fig. 40 for the uncertainty breakdown).

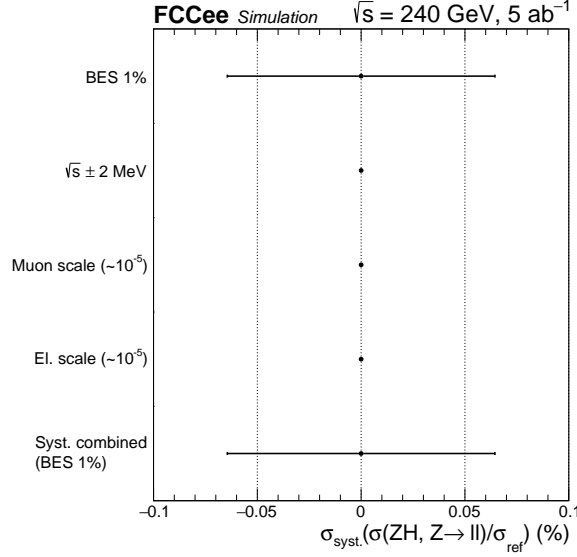


Fig. 40 Uncertainty breakdown on the cross-section analysis.

5.3 Conclusion

A BDT approach has been introduced to replace the $\cos(\theta_{\text{miss}})$ cut to ensure the model-independency of the ZH cross-section measurement. Binned fits are applied on both m_{rec} and BDT score distributions to obtain the uncertainties on the cross-section measurements.

Removing the $\cos(\theta_{\text{miss}})$ cut increases the uncertainty on the ZH cross-section by 61 % (0.74 % to 1.19 %).

Changing the fit distribution from m_{rec} to the BDT score distribution, the uncertainty on the ZH cross-section is improved from 1.19 % to 0.80 %. It becomes comparable to the result obtained when fitting on m_{rec} with the model-dependent baseline selection (0.74 %), while the model independency is preserved.

The final result is predominantly due to the $\mu^+\mu^-$ channel, with the electron-electron channel contributing to a 23 % improvement.

6 Sources of systematic uncertainties

In this section, the main sources of systematic uncertainties are addressed, and their impact on both the cross-section and mass measurements is estimated. Several sources of systematic uncertainty must be taken into account when building the test statistic used to extract the proper uncertainties on the Higgs mass and cross-section. Such sources are modeled in the test statistic as nuisance parameters, with the effect of either changing the event rate of the considered signal and background processes (rate uncertainties) or changing the shape of the recoil mass template distributions (shape uncertainties). Depending on their type, experimental and theoretical uncertainties are propagated as shape or normalization uncertainties to the recoil mass and eventual other distributions such as control regions.

Nuisances are propagated to the Likelihood by Gaussian constraint terms centered around their zero-values (i.e. $\mu = 0$). The magnitude of the uncertainty, being the width σ that enters the Gaussian constraint term, is estimated by an educated guess or by additional studies. For each of the relevant systematics, their magnitude is estimated in this section. The impact of the nuisances and the breakdown are discussed in the relevant sections for the mass and cross-section.

Note that not all uncertainties are implemented yet in the fit. In particular, ISR, FSR, lepton resolution, signal and background modeling uncertainties have to be evaluated more precisely before being implemented in these analyses.

6.1 Beam Energy Spread (BES)

At a center-of-mass energy of $\sqrt{s} = 240$ GeV, the nominal (Gaussian) beam energy spread is equal $\pm 0.185\%$ per beam, or equivalently 222 MeV (cfr. CDR). This energy spread is enabled in the WHIZARD and Pythia event generators as independent Gaussian smearings². The effect on the final recoil distribution is shown in Figure 41. A significant broadening of the mass peak is observed.

The beam energy spread is subject to uncertainties related to the accelerator equipment (RF cavities and monitoring). As the BES has an impact on the recoil mass peak, it is important to quantify this effect and estimate the impact on the mass and cross-section measurements. We describe two methods to estimate the uncertainty of the BES:

1. Accelerator instrumentation: the bunch length can be monitored at the ps level or better, which is equivalent to $c \times 1$ ps = 0.3 mm. Since the bunch length at $\sqrt{s} = 240$ GeV is 5.3 mm, this corresponds to a beam energy spread uncertainty of about $0.3 / 5.3 = 6\%$ (or better).
2. Data-driven: using $ee \rightarrow f\bar{f}(\gamma)$ events by measuring the longitudinal imbalance of di-muon spectrum and/or Bhabha during the fill. This could constrain the BES uncertainty to 1 %.

²In Pythia 8.X.X, both beam smearings are varied simultaneously.

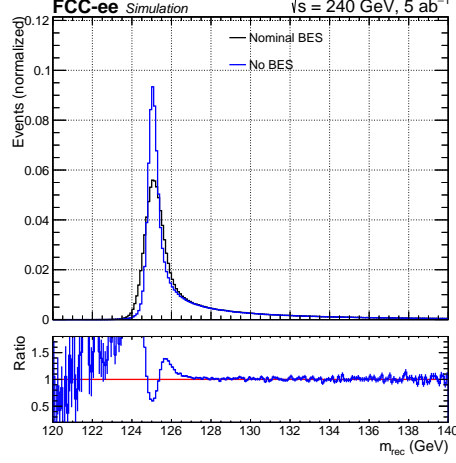


Fig. 41 Effect of the beam energy spread (0 and 222 MeV) on the $Z(\mu, \mu)H$ recoil mass distribution.

In order to assess the impact of the BES uncertainties on the recoil mass distribution, two perturbed signals at the nominal Higgs mass value of 125 GeV were generated with $\pm 6\%$ and $\pm 1\%$ of BES uncertainty respectively w.r.t. the nominal BES value. The results and ratios w.r.t. the nominal are shown in Figure 42. For the $\pm 6\%$ variations, a shape effect of 1-2 % is observed near the mass peak, whereas the impact on the $\pm 1\%$ variations is reduced substantially.

The perturbed samples are fitted with the 2CBG PDF where the norm, CB μ , and CB σ are free parameters, keeping the other parameters as their nominal values derived from the central sample (nominal BES).

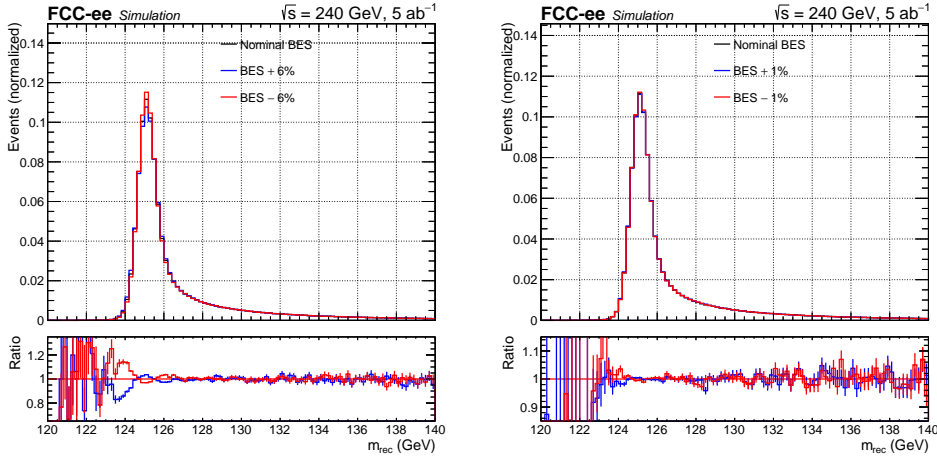


Fig. 42 Effect of the beam energy spread uncertainty ($\pm 6\%$ left, $\pm 1\%$ right) on the $Z(\mu, \mu)H$ recoil mass distribution.

6.2 Initial State Radiation (ISR)

Initial State Radiation uncertainties arise from the mis-modeling of the ISR spectra in Monte-Carlo generators. It mainly affects the high-mass tails of the recoil mass distribution as can be seen from Figure 43 (left) where the comparison has been made between switching ON and OFF the ISR uncertainty in **WHIZARD**. Apart from a small shift of the peak, the distribution broadens and the effect becomes more important in the high-mass tail of the distribution, as can be expected from the recoil mass formula.

The main goal is to derive a valid (shape) uncertainty for the ISR spectra, in order to evaluate its impact on the mass and cross-section measurements. Estimating the ISR uncertainty by taking the ISR OFF distribution is too drastic (cf. Figure 43) and will yield a large overestimation of the ISR uncertainty. Therefore, in the next paragraph, the ISR uncertainty with **WHIZARD** will be re-evaluated. Afterward, **WHIZARD** will be compared to the state-of-the-art **KKMC** Monte-Carlo generator.

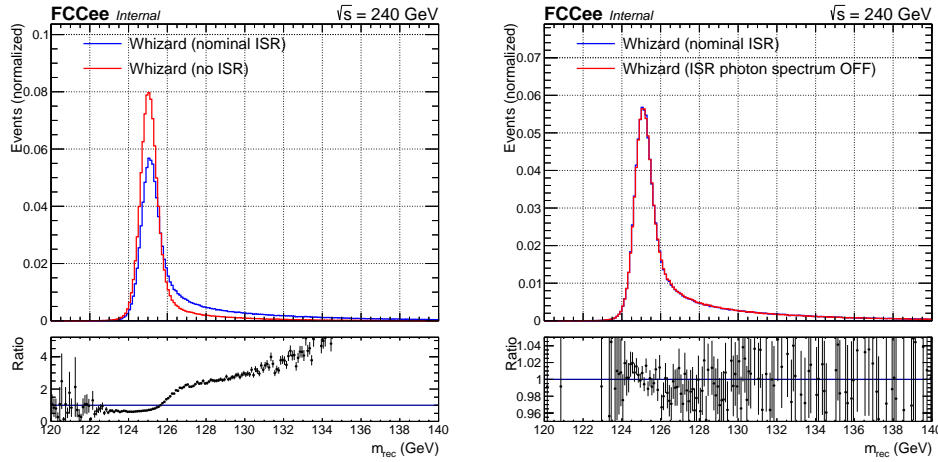


Fig. 43 Effect on the recoil mass distribution by switching OFF the ISR treatment (left) and by switching OFF the photon spectrum only (right).

As the **WHIZARD** ISR spectrum is quasi-identical to **KKMC** (see later) and there is a lack of handles to perturb the ISR in **WHIZARD**, currently ISR is not included as a systematic uncertainty.

6.2.1 ISR treatment in **WHIZARD**

There are two handles in **WHIZARD** to treat ISR uncertainty:

1. Order of the QED radiation approximation;
2. Binary flag related to giving a non-zero p_T spectrum to the photons (strict colinear approximation). An ad-hoc distribution for the photon spectrum is applied.

The effect on the latter, by switching OFF the photon p_T spectrum is shown in Figure 43 (right). A strong shape dependency is observed around the mass peak, but also on the tails despite being hardly visible due to the large statistical error bars.

This perturbed distribution was used to evaluate the impact of the ISR uncertainty on the mass and cross-section. The distribution is symmetrized around the central one (i.e. with nominal ISR). It was found that the impact is quite large due to its strong shape dependency, therefore this approach is very conservative. It is believed that the theoretical ISR uncertainties are much lower and more studies are to be performed to further reduce this uncertainty to a reasonable level.

6.2.2 Comparison with KKMC

KKMC is a state-of-the-art Monte-Carlo generator for $ee \rightarrow f\bar{f}$ production, where the ISR treatment is known to be modeled properly. A comparison has been made between KKMC and WHIZARD in the $ee \rightarrow \mu\mu$ at $\sqrt{s} = 240$ GeV with ISR enabled but BES and FSR disabled, in order to assess only the ISR performance in WHIZARD (in this configuration all photons come from ISR).

In Figure 44, the sum of all the photon momenta (left) and the di-muon momentum (right) is shown, both of which are ISR-sensitive distributions, as a comparison between both event generators. Only the generator-level quantities are shown here. The cuts for these distributions are simple: exactly two opposite sign leptons with $m(\mu^+\mu^-) > 220$ GeV, to be in the same ISR-kinematical regime as the $e^+ + e^- \rightarrow ZH$ process. WHIZARD is producing distributions statistically compatible with the KKMC ones, therefore the ISR treatment in WHIZARD can be considered as accurate and valid. A slight trend in the high $p(\mu^+\mu^-)$ tail is observed, though within statistical uncertainty.

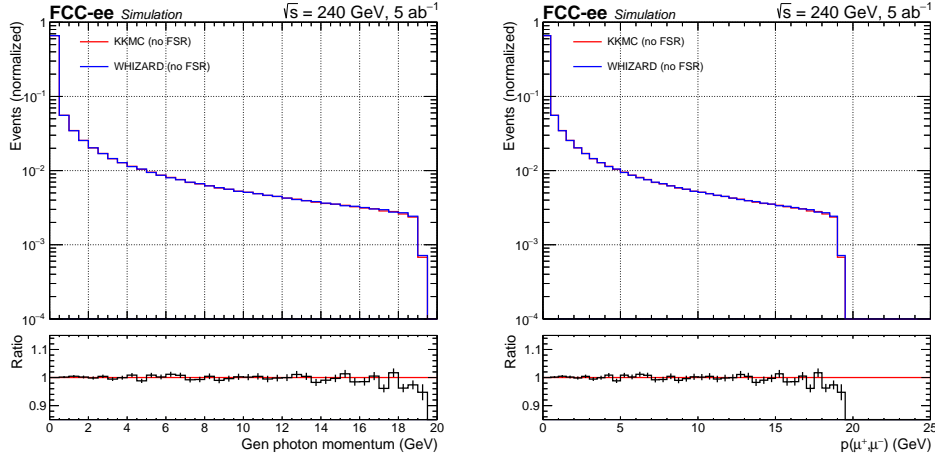


Fig. 44 Comparison between KKMC and WHIZARD with ISR enabled but BES and FSR OFF. Exactly two opposite-sign leptons are required with $m(\mu^+\mu^-) > 220$ GeV.

776 6.3 Center-of-mass (COM)

777 The center-of-mass energy at $\sqrt{s} = 240$ GeV is expected to be known at the 2 MeV
 778 level or better. It will be measured precisely using radiative return events in the
 779 $Z \rightarrow \mu\mu$ or $Z \rightarrow jj$ channels. As \sqrt{s} enters directly into the recoil mass definition, the
 780 impact of this uncertainty translates directly into a 2 MeV systematic uncertainty on
 781 the fitted mass. The change on the cross-section is expected to be negligible.

782 From the definition of the recoil mass (with E_i the energy of lepton i),

$$m_{rec}^2 = s - 2\sqrt{s}(E_1 + E_2) + m_{ll}^2 \quad (6)$$

783 and assuming $E_1 + E_2 = m_Z$ and $m_{rec} = m_H$ one obtains $E_1 + E_2 = (s + m_Z^2 -$
 784 $m_H^2)/(2\sqrt{s})$. If \sqrt{s} differs with an amount of δ , one has:

$$m_{rec}^2 = (\sqrt{s} + \delta)^2 - 2(\sqrt{s} + \delta)(s + m_Z^2 - m_H^2)/(2\sqrt{s}) + m_{ll}^2. \quad (7)$$

785 Taking the differential:

$$d(m_{rec}^2) = \delta(s - m_Z^2 + m_H^2)/(2\sqrt{s}), \quad (8)$$

786 which numerically yields $d(m_{rec}) = 1.08 * \delta * 125 \text{ GeV}/m_{rec}$ (note that 1.08 would
 787 be 1.0 if we were exactly at the threshold). Finally, if the center-of-mass is shifted
 788 by 2 MeV ($= \delta$), the corresponding variation on $d(m_{rec}) = 2.16$ MeV. This simple
 789 calculation assumes no shape variation but rather a shift of the recoil mass peak.
 790 However, nearly all the statistics are within ± 1 GeV of the peak, such that the shift
 791 can be considered as constant within 1 %.

792 The perturbed samples are fitted with the 2CBG PDF where the norm, CB μ , and CB
 793 σ are free parameters, keeping the other parameters as their nominal values derived
 794 from the central sample (nominal BES).

795 6.4 Lepton momentum scale (LEPSCALE)

796 The lepton momentum scale can safely be assumed to be in the order of 10^{-5} due to
 797 the large statistical power of radiative return events which could constrain the lepton
 798 scale up to this precision.

799 Indeed, with 5 ab^{-1} of data at $\sqrt{s} = 240$ GeV, we will have about 100 M of Z bosons
 800 from the radiative return, hence 3 M (per lepton flavor) of $Z \rightarrow \ell\ell$ that can be used
 801 to calibrate the scale. The resolution on the $Z \rightarrow \ell\ell$ mass peak is about 150-200

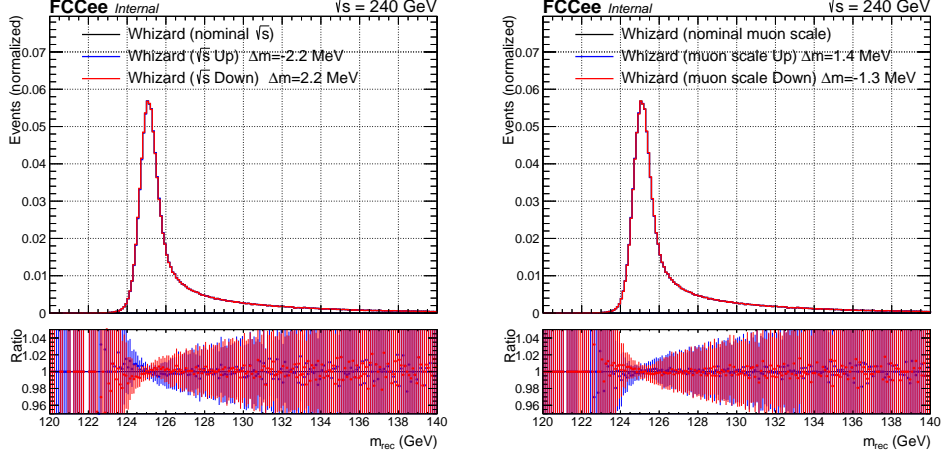


Fig. 45 Effect on the recoil mass when perturbing the center-of-mass energy with 2 MeV (left) and the muon momentum scale (right). The quoted Δm values are the mean histogram values w.r.t. the nominal sample. Plots are done using the Spring2021 campaign.

MeV, hence an uncertainty on the peak position of $200 \text{ MeV} / \sqrt{3 \times 10^6} = 0.11 \text{ MeV}$. Hence there is the statistical potential to determine in-situ the scale with a relative uncertainty of $0.11 \text{ MeV} / 90 \text{ GeV} = 10^{-6}$, comparable to the (by then) relative uncertainty on the Z mass. However, since it is not proven yet that the stability of the magnetic field can be controlled to the level of 10^{-6} or better, we can take 10^{-5} as a conservative estimate (NMR probes should allow monitoring of the field to that level). One may also want to check the (theta, phi) dependence of the scale, but the calibration runs at the Z peak will provide a high level of precision.

To understand the effect on the recoil mass, one needs to change the lepton energies by $\delta = 10^{-5} \times E$, with $E \approx 45 \text{ GeV}$ since the Z is nearly at rest. Writing that $m_{ll} \approx E_1 + E_2$, one obtains that $d(m_{rec}^2) = 4 * \delta * (\sqrt{s} - m_Z)$, which yields in the peak region $d(m_{rec}) = 2 * \delta * 150/125 = 1 \text{ MeV}$.

This simple error propagation gives a resulting uncertainty of 1 MeV on the mass. This is checked in the analysis by changing the lepton energy with a factor of 10^{-5} and checking the resulting recoil distribution. Indeed, the impact on the fit with the perturbed momentum scale results in an uncertainty of approximately 1 MeV for both muons and electrons.

Because the lepton scale is independent of muons and electrons (they are measured in independent event phase spaces), the muon and electron momentum scale are de-correlated in the fit.

The resulting varied scale profiles are used as shape uncertainties in the fit. The perturbed samples are fitted with the 2CBG PDF where the norm, CB μ , and CB σ are free parameters, keeping the other parameters as their nominal values derived from the central sample (nominal BES).

826 **6.5 Lepton momentum resolution (LEPRES)**

827 Uncertainty related to the muon momentum resolution must be taken into account.
828 It directly affects the width of the recoil distribution, hence the precision of how the
829 Higgs mass can be resolved. Resolution stability and uncertainties are extracted from
830 $Z \rightarrow \ell\ell$ events, as discussed in the previous paragraph. The uncertainty has to be
831 propagated to the analysis and the impact has to be estimated.

832 **6.6 Final State Radiation (FSR)**

833 By default, QED Final State Radiation (FSR) is performed by `PYTHIA`. However, the
834 `KKMC` FSR implementation is more state-of-the-art as it has an implementation of
835 `PHOTOS` which is fine-tuned mostly to LEP data. An uncertainty of the FSR spectra
836 between `KKMC` and `WHIZARD` has to be implemented and propagated to the fit.

837 **6.7 Signal modeling (SIGM)**

838 A systematic uncertainty to take into account the signal modeling has to be
839 implemented in the fit.

840 **6.8 Background modeling (BKGM)**

841 A systematic uncertainty to take into account the background modeling has to be
842 implemented in the fit.

7 Experimental requirements

In this section, a summary of the detector requirements is given, which are mainly applicable to the mass analysis.

An ultimate precision on the Higgs mass below 4 MeV is achievable with an integrated luminosity of 5 ab^{-1} and using the improved IDEA detector, consisting of a very light drift chamber and crystal electromagnetic calorimeter. It has been shown that the uncertainty on the Higgs mass is statistically limited, with an impact of the experimental uncertainties less than 10 %. However, considering the option of 4 interaction points leading to an integrated luminosity of 10 ab^{-1} , the difference between the statistical and systematic uncertainties would become smaller. This imposes more strict experimental requirements in order to keep the systematic component as small as possible compared to the statistical uncertainty.

The muon channel is dominant in the mass uncertainty, therefore an excellent tracking performance is a key detector requirement for this analysis. Thanks to the drift chamber, resolutions at the sub-percent level are achievable, depending on the momentum and position in the detector. As shown, when replacing the reconstructed muons with their associated generator kinematics, this "ideal" muon resolution improves the uncertainty by 30 %, including the selection requirements and backgrounds included. When increasing the magnetic field from 2T to 3T, the uncertainty mildly increases with only 15 %, limited by the beam energy spread which becomes dominant. Given the extra expected complications regarding the machine-detector interface and luminosity control upon increasing the magnetic field, such an option is not favored in the detector design. Categorization of the events in distinct azimuthal regions decouples the different resolutions of the forward and central regions, leading to an improvement of 20 %.

On the other hand, the electron channel improves the uncertainty by 25 %, which is less than the statistically achievable improvement of 41 %. This is primarily due to the worse momentum resolution of the electrons, rather than the increase of the Z/γ t-channel background. Nevertheless, the 25 % improvement is due to the crystal calorimeter which has an excellent resolution for low energy photons, such that the Bremsstrahlung photons can be recovered, leading to a global electron momentum resolution that is "only" 25 % worse than the one from muons. This somewhat ideal detector scenario is studied by degrading the electron momentum resolution by a factor of 2 w.r.t. the muons, leading to an overall degradation of the Higgs mass of 5 % w.r.t. the nominal detector configuration.

The beam energy spread of 222 MeV contributes strongly to the broadening of the recoil distribution. The associated uncertainty, estimated by data-driven techniques, is 1 %, which amounts to a few MeV on the beam energy uncertainty. The resulting uncertainty on the Higgs mass is negligible. To assess the impact on the beam energy spread itself, a study has been performed by switching off entirely the beam energy spread, which concluded in an improvement of about 50 % on the Higgs mass uncertainty.

885 A dominating systematic uncertainty originates from the precision of the center-of-
 886 mass energy \sqrt{s} , which directly enters the recoil mass definition. Data-driven estimates
 887 show that this can be controlled up to a 2 MeV level, but more rigorous studies have
 888 to be performed. After implementing such uncertainty in the fit, the impact on the
 889 Higgs mass was found to be 2 MeV, as expected, which serves as a validation of the
 890 methods and fit strategies used.

891 **8 Conclusion**

892 In this note, the Higgs boson mass and the model-independent ZH cross-section mea-
 893 surements have been studied using di-muon and di-electron events, using the recoil
 894 mass method, with the FCC-ee simulated data at $\sqrt{s} = 240$ GeV. First, a basic
 895 event selection is applied to reduce the main backgrounds while retaining the signal
 896 yields. The cross-section measurement then proceeds using a dedicated Boosted Deci-
 897 sion Tree to further separate the signal from backgrounds, with emphasis on Higgs
 898 decay mode independence. The di-electron and di-muon final states are fitted simul-
 899 taneously to extract the ZH cross-section with a relative precision of 0.80 %. Instead
 900 of the BDT, the Higgs mass analysis uses an additional kinematic cut to reduce the
 901 background: the Higgs mass is measured by fitting directly the recoil mass distribu-
 902 tion, after imposing an additional selection on $\cos(\theta_{\text{miss}})$. The recoil mass distributions
 903 are modeled analytically using a custom PDF and are injected into a maximum like-
 904 lihood fit to extract the mass uncertainty. By categorizing the leptons based on their
 905 azimuthal angle, the sensitivity is increased and a combined uncertainty of 4.43 MeV
 906 is obtained when including the dominant systematics. Several systematic uncertainties
 907 have been evaluated and found to be almost negligible for the cross-section measure-
 908 ment, but impacting the Higgs mass uncertainty at the 10 % level. An extensive set of
 909 experimental requirements have been discussed, both from the machine and detector
 910 point of view, and the conclusion is that the tracking performance and the center-of-
 911 mass determination are the most crucial elements. They must be controlled precisely
 912 to achieve the final precision that the statistics that will be delivered by FCC-ee is
 913 promising.

Appendix A Event selection plots

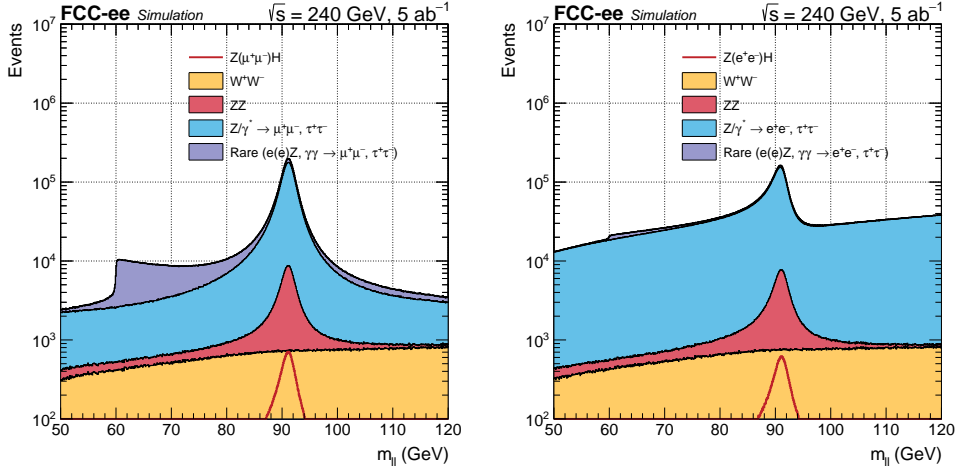


Fig. A1 $m_{\ell\ell}$ distribution after the muon selection criteria for the muon (left) and electron (right) final states.

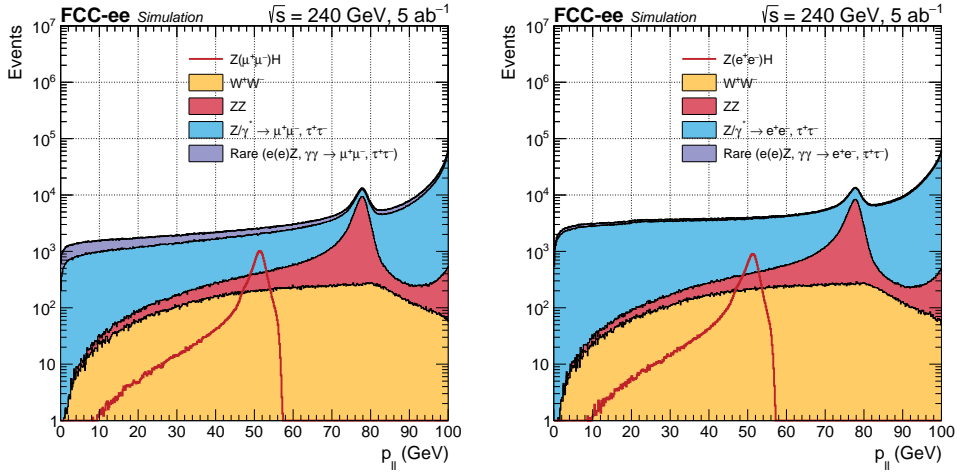


Fig. A2 $p_{\ell\ell}$ distribution after the $m_{\ell\ell}$ cut for the muon (left) and electron (right) final states.

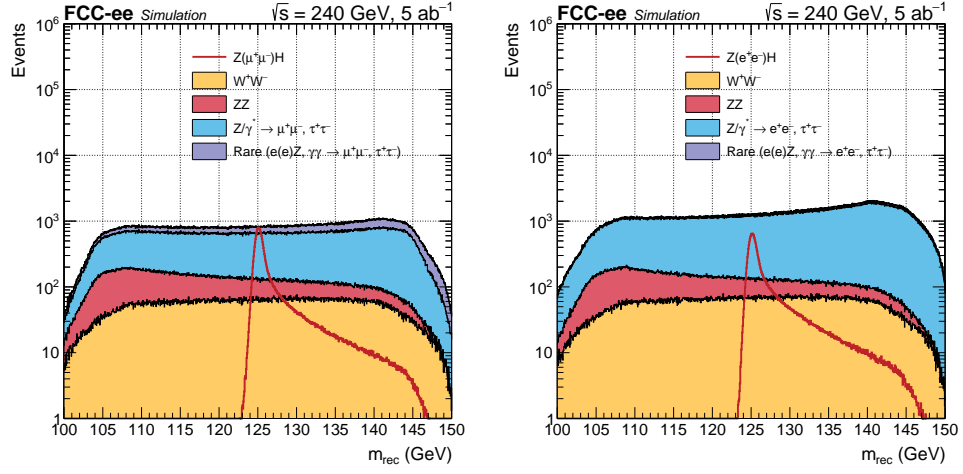


Fig. A3 m_{rec} distribution after the $p_{\ell\ell}$ cut for the muon (left) and electron (right) final states.

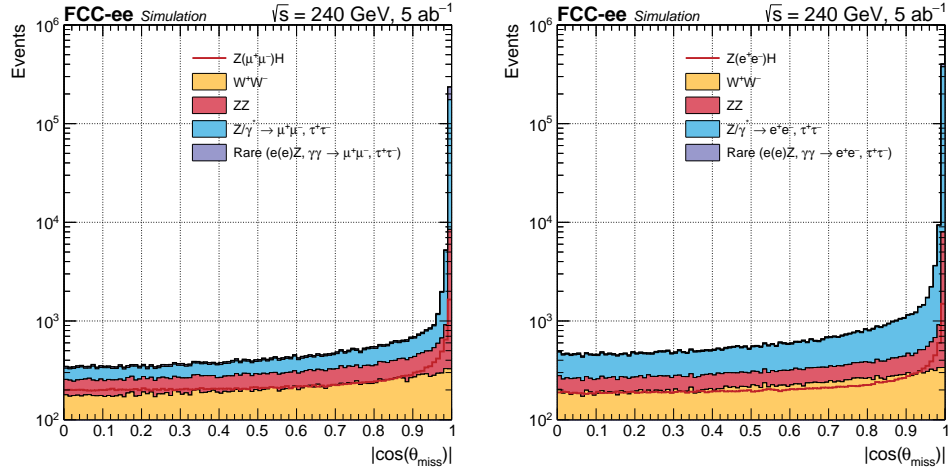


Fig. A4 $\cos(\theta_{\text{miss}})$ distribution after the m_{rec} cut for the muon (left) and electron (right) final states.

Appendix B Recoil mass fits

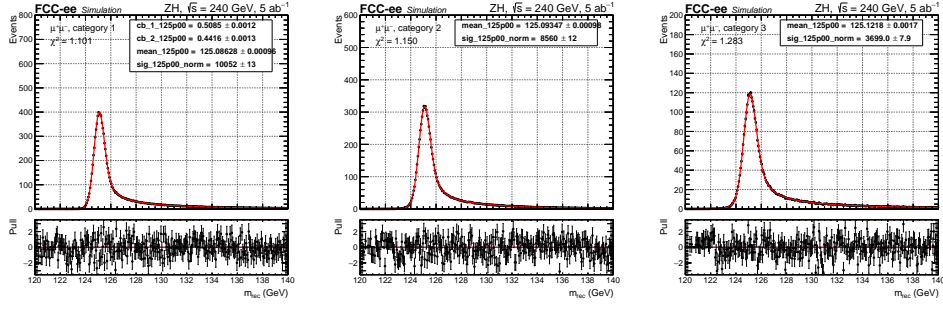


Fig. B5 Signal samples for 125 GeV muon channel: CC (left), CF (middle) FF (right).

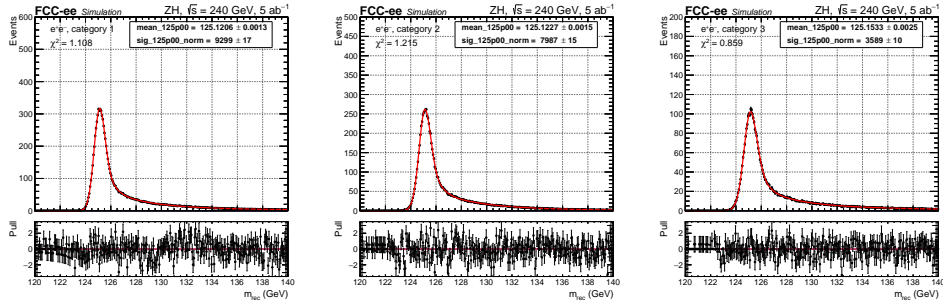


Fig. B6 Signal samples for 125 GeV electron channel: CC (left), CF (middle) FF (right).

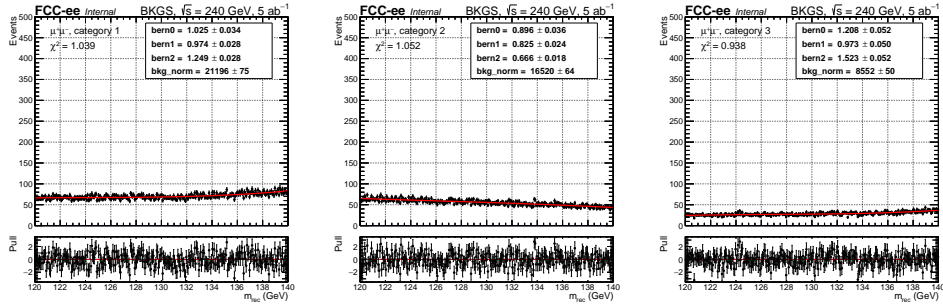


Fig. B7 Background distributions for the muon channel: CC (left), CF (middle) FF (right).

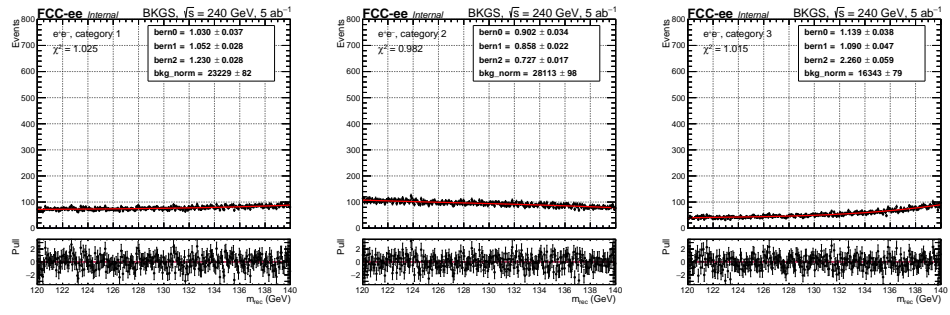


Fig. B8 Background distributions for the electron channel: CC (left), CF (middle) FF (right).

Appendix C BDT input variables

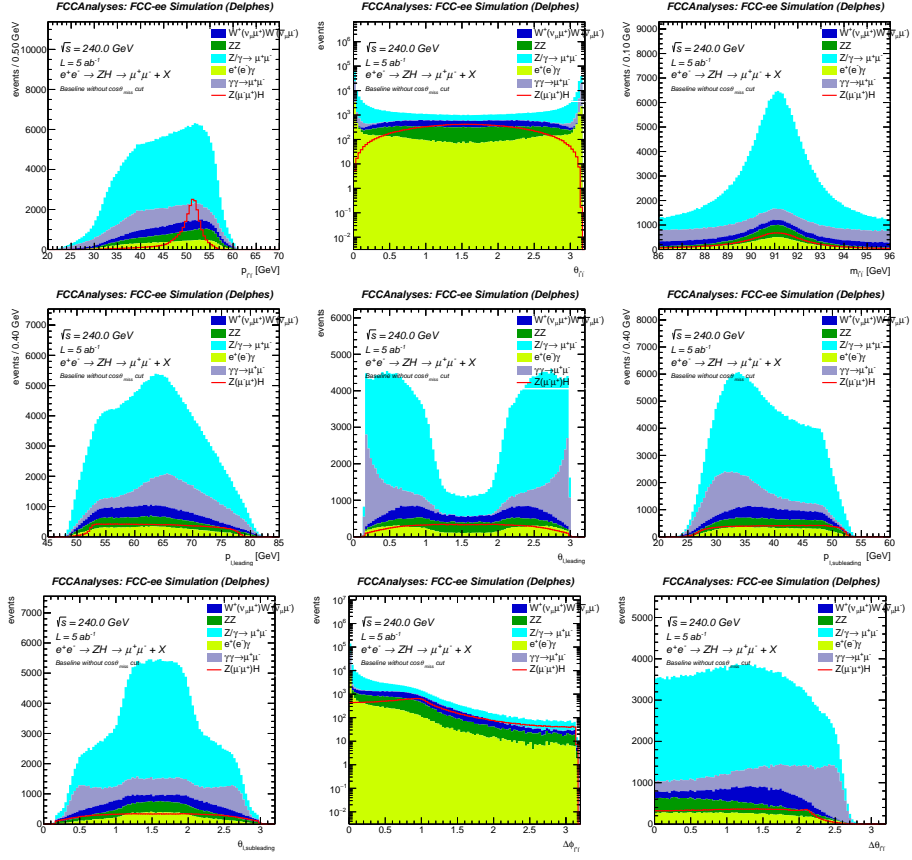


Fig. C9 Input variables for BDT training for the $\mu^+\mu^-$ channel.

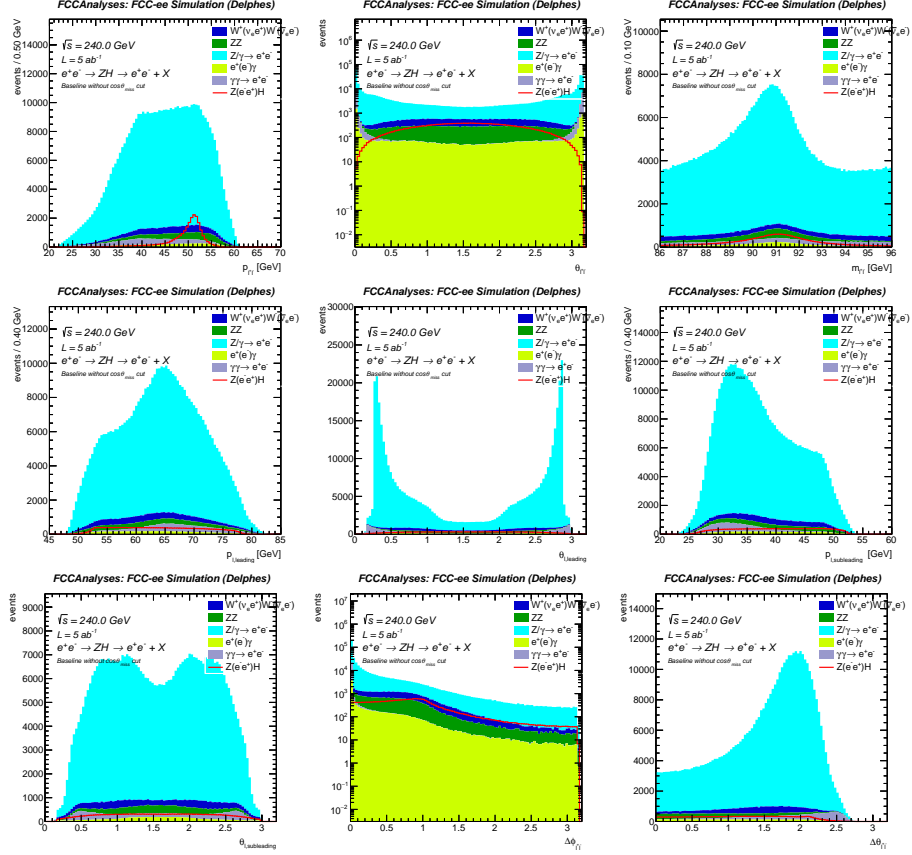


Fig. C10 Input variables for BDT training for the e^+e^- channel.

917 Appendix D BDT hyper-parameters

918 Each hyper-parameter and its respective value are elaborated as follows:

- 919 1. **n_estimators (350)**: This parameter refers to the number of boosting rounds or
920 the number of trees used in the model. A higher value typically results in better
921 model performance but may also lead to over-fitting. In our case, we have chosen
922 350 trees to balance model performance and computational efficiency.
- 923 2. **learning_rate (0.20)**: The learning rate, also known as shrinkage, controls the con-
924 tribution of each tree to the final model. A smaller learning rate typically requires
925 more trees but reduces the risk of over-fitting. We have set the learning rate to
926 0.20, which provides a good balance between model performance and the number
927 of trees needed.
- 928 3. **max_depth (3)**: The maximum depth of each tree determines the number of layers
929 in the tree. A larger depth increases the model's complexity and may result in better
930 performance but also increases the risk of over-fitting. We have set the maximum
931 depth to 3, which provides a reasonable trade-off between model complexity and
932 the risk of over-fitting.
- 933 4. **subsample (0.5)**: This parameter controls the fraction of the training data-set
934 used to build each tree. A lower value introduces randomness and may help prevent
935 over-fitting. In our case, we have set the sub-sample ratio to 0.5, meaning that each
936 tree is built using a randomly selected 50% of the training data.
- 937 5. **gamma (3)**: The gamma parameter, also known as the minimum loss reduction,
938 specifies the minimum reduction in the loss function required to make a split at
939 a leaf node. A higher gamma value makes the model more conservative, reducing
940 the risk of over-fitting. We have set gamma to 3, which helps control the model's
941 complexity while still allowing it to learn from the data.
- 942 6. **min_child_weight (10)**: This parameter controls the minimum sum of instance
943 weights (hessians) required in a child node. Larger values of min_child_weight
944 result in a more conservative model by preventing over-fitting. We have set
945 the min_child_weight value to 10 to control the model's complexity and avoid
946 over-fitting.
- 947 7. **max_delta_step (0)**: This parameter sets the maximum step size allowed for each
948 tree's weight estimation. A value of 0 means that there is no constraint on the step
949 size. In our case, we have set max_delta_step to 0, allowing the model to adjust the
950 step size freely.
- 951 8. **colsample_bytree (0.5)**: This parameter controls the fraction of features to be
952 randomly selected for each tree. A smaller value can help prevent over-fitting by
953 reducing the correlation between trees. We have set the colsample_bytree value to
954 0.5, meaning that each tree is built using a random 50% of the features.

References

- [1] M. Benedikt, et al., FCC-ee: The Lepton Collider : Future Circular Collider Conceptual Design Report Volume 2. Eur. Phys. J. Spec. Top. **228**(261), 400 (2019). <https://doi.org/10.1140/epjst/e2019-900045-4>
- [2] M. Aaboud, et al., Observation of $H \rightarrow b\bar{b}$ decays and VH production with the ATLAS detector. Phys. Lett. B **786**, 59–86 (2018). <https://doi.org/10.1016/j.physletb.2018.09.013>. [arXiv:1808.08238](https://arxiv.org/abs/1808.08238) [hep-ex]
- [3] A.M. Sirunyan, et al., Observation of Higgs boson decay to bottom quarks. Phys. Rev. Lett. **121**(12), 121801 (2018). <https://doi.org/10.1103/PhysRevLett.121.121801>. [arXiv:1808.08242](https://arxiv.org/abs/1808.08242) [hep-ex]
- [4] P. Azzurri, G. Bernardi, S. Braibant, D. d’Enterria, J. Eysermans, P. Janot, A. Li, E. Perez, A special Higgs challenge: measuring the mass and production cross section with ultimate precision at FCC-ee. Eur. Phys. J. Plus **137**(1), 23 (2022). <https://doi.org/10.1140/epjp/s13360-021-02202-4>. [arXiv:2106.15438](https://arxiv.org/abs/2106.15438) [hep-ex]
- [5] F.A. Berends, R. Kleiss, Initial State Radiation at LEP Energies and the Corrections to Higgs Boson Production. Nucl. Phys. B **260**, 32–60 (1985). [https://doi.org/10.1016/0550-3213\(85\)90309-8](https://doi.org/10.1016/0550-3213(85)90309-8)
- [6] G. Altarelli, T. Sjostrand, F. Zwirner (eds.). *Physics at LEP2: Vol. 1*, CERN Yellow Reports: Conference Proceedings (1996). <https://doi.org/10.5170/CERN-1996-001-V-1>
- [7] M. Cepeda, et al., Report from Working Group 2: Higgs Physics at the HL-LHC and HE-LHC. CERN Yellow Rep. Monogr. **7**, 221–584 (2019). <https://doi.org/10.23731/CYRM-2019-007.221>. [arXiv:1902.00134](https://arxiv.org/abs/1902.00134) [hep-ph]
- [8] D. d’Enterria, Higgs physics at the Future Circular Collider. [arXiv \(2017\). arXiv:1701.02663](https://arxiv.org/abs/1701.02663) [hep-ex]
- [9] R.L. Workman, et al., Review of Particle Physics. PTEP **2022**, 083C01 (2022). <https://doi.org/10.1093/ptep/ptac097>
- [10] A. Li, Perspectives for Higgs measurements at Future Circular Colliders. PoS **PANIC2021**, 420 (2022). <https://doi.org/10.22323/1.380.0420>
- [11] J. de Favereau, C. Delaere, P. Demin, A. Giammanco, V. Lemaître, A. Mertens, M. Selvaggi, DELPHES 3, A modular framework for fast simulation of a generic collider experiment. JHEP **02**, 057 (2014). [https://doi.org/10.1007/JHEP02\(2014\)057](https://doi.org/10.1007/JHEP02(2014)057). [arXiv:1307.6346](https://arxiv.org/abs/1307.6346) [hep-ex]
- [12] W. Kilian, T. Ohl, J. Reuter, WHIZARD: Simulating Multi-Particle Processes at LHC and ILC. Eur. Phys. J. C **71**, 1742 (2011). <https://doi.org/10.1140/epjc/s10052-011-1742-y>. [arXiv:0708.4233](https://arxiv.org/abs/0708.4233) [hep-ph]

- 991 [13] T. Sjostrand, S. Mrenna, P.Z. Skands, PYTHIA 6.4 Physics and Manual. JHEP
992 **05**, 026 (2006). <https://doi.org/10.1088/1126-6708/2006/05/026>. arXiv:hep-
993 [ph/0603175](https://arxiv.org/abs/hep-ph/0603175)
- 994 [14] T. Sjöstrand, S. Ask, J.R. Christiansen, R. Corke, N. Desai, P. Ilten, S. Mrenna,
995 S. Prestel, C.O. Rasmussen, P.Z. Skands, An introduction to PYTHIA 8.2. Com-
996 put. Phys. Commun. **191**, 159–177 (2015). [https://doi.org/10.1016/j.cpc.2015.](https://doi.org/10.1016/j.cpc.2015.01.024)
997 [01.024](https://doi.org/10.1016/j.cpc.2015.01.024). arXiv:1410.3012 [hep-ph]
- 998 [15] S. Jadach, B.F.L. Ward, Z. Was, S.A. Yost, A. Siodmok, Multi-photon Monte
999 Carlo event generator KKMCEE for lepton and quark pair production in lepton
1000 colliders. Comput. Phys. Commun. **283**, 108556 (2023). [https://doi.org/10.1016/](https://doi.org/10.1016/j.cpc.2022.108556)
1001 [j.cpc.2022.108556](https://doi.org/10.1016/j.cpc.2022.108556). arXiv:2204.11949 [hep-ph]
- 1002 [16] K. Hagiwara, H. Iwasaki, A. Miyamoto, H. Murayama, D. Zeppenfeld, Single weak
1003 boson production at TeV e+ e- colliders. Nucl. Phys. B **365**, 544–596 (1991).
1004 [https://doi.org/10.1016/0550-3213\(91\)90442-Z](https://doi.org/10.1016/0550-3213(91)90442-Z)
- 1005 [17] B.P. Roe, H.J. Yang, J. Zhu, Y. Liu, I. Stancu, G. McGregor, Boosted
1006 decision trees, an alternative to artificial neural networks. Nucl. Instrum.
1007 Meth. A **543**(2-3), 577–584 (2005). <https://doi.org/10.1016/j.nima.2004.12.018>.
1008 [arXiv:physics/0408124](https://arxiv.org/abs/physics/0408124)
- 1009 [18] T. Chen, C. Guestrin, in *Proceedings of the 22nd ACM SIGKDD International*
1010 *Conference on Knowledge Discovery and Data Mining* (ACM, New York, NY,
1011 USA, 2016), KDD '16, pp. 785–794. <https://doi.org/10.1145/2939672.2939785>.
1012 URL <http://doi.acm.org/10.1145/2939672.2939785>